Seasonality and forcing factors of the Alaskan Coastal Current in the Bering Strait from July 2011 to July 2012

Brett Alexander Morris

A thesis
submitted in partial fulfillment of the
requirements for the degree of

Master of Science

University of Washington
2019
Committee:
Rebecca Woodgate
Parker MacCready
Jodi Young

Program Authorized to Offer Degree:
College of the Environment

University of Washington

Abstract

Seasonality and forcing factors of the Alaskan Coastal Current in the Bering Strait from July 2011 to July 2012

Brett Alexander Morris

Chair of the Supervisory Committee:
Rebecca Woodgate
School of Oceanography

A relatively narrow (~85km) and shallow (~50m) Bering Strait is the only connection between the Pacific and Arctic oceans. Flow through this strait dominates water properties of the Chukchi Sea, impacts Arctic sea ice and stratification, and may influence global climate through freshwater input to the sinking zones of the global thermohaline circulation.

A buoyant coastal current, the Alaskan Coastal Current (ACC), typically present in the eastern Bering Strait from approximately late April to late December, contributes significantly to the total heat and freshwater fluxes through the strait, (adding approximately 10^{20}J/yr of heat (T_{ref}=-1.9ºC) and 600km^3/yr of freshwater (S_{ref}=34.8psu)), and drives much of the spatial variability in water properties in the eastern Chukchi Sea. However, the seasonal variability of this current has not yet been quantified in any detail. We use temperature, salinity, and velocity data from a 6-mooring array deployed across the eastern channel of the Bering Strait from July 2011 to July 2012 to study the seasonality and driving mechanisms of the ACC.

We find the ACC is present (and flowing strongly) in July 2011, but disappears from the strait in November 2011. It starts to reappear in May 2012, and is well established by July 2012. Building on the known high correlation between flow and local wind (r~0.7), we examine a single value decomposition of the meridional velocity flow structure in the strait and see that the dominant mode (59% of the variance) contains a strong surface intensified signal trapped to the eastern coast reminiscent of the ACC.

Through the use of a simple linear interpolation "box" method, we improve previous transport estimates during the months of strongest ACC transport by ~34%. Using this analysis, we find the greatest monthly mean of ACC transport is in August 2011 at 0.44 ± 0.06 Sv, equivalent to ~29% of the entire Bering Strait throughflow. At the ACC's peak in August 2011, mooring data suggests its monthly mean salinity was at least 2.1 psu fresher and 3.9 ºC warmer than the main Bering Strait throughflow, although summer hydrographic sections suggest this is an underestimate, likely because the upper mooring instrumentation is ~18 m below the surface.

We compare many parameters from theoretical studies of buoyant coastal currents (with or without wind forcing) with the mooring observations and conclude that our observations poorly constrain the current's width and many different theories poorly estimate the current's depth. Theory also suggests that the ACC is mainly driven by buoyancy forcing rather than wind forcing.

We present an in-depth analysis on three different ways that wind forcing can impact a buoyant coastal current, viz., separation from the coast, flow reversals, and isopycnal tilting. We find that theory from Csanady (1977) successfully predicts ACC separation from the coast during strong southward wind events, consistent with separation observed in hydrographic data from August 2018. Additionally, we find an approximately 8 m/s southward wind is required to reverse flow of the ACC, and finally that two different theoretical parameters for estimating isopycnal tilting time bound observations, with the parameter t_a from Moffat and Lentz (2012) being more accurate than t_{tilt} from Whitney and Garvine (2005).

Data from the United States Geological Survey shows the Yukon River discharge is most highly correlated (r=0.76) to ACC freshwater transport with a 12-15 day lag, and that the Yukon River discharge, combined with other rivers from the Alaskan peninsula, as well as the Unimak Pass freshwater discharge, are all probable ACC freshwater sources.

Table of Contents

List of Figures……………………………………………………………………………3

List of Tables……………………………………………………………………………5

1.1 Characteristics of the Bering Strait Region 6

1.2 Importance of understanding the Bering Strait for global circulation and climate change and solving real world problem 11

1.3 Theoretical framework for a Buoyant Coastal Current (BCC) 12

1.4 Wind's influence on a Buoyant Coastal Current 16

2.1: Introduction to moored data 21

2.2: Mooring array location and instrumentation 22

2.3: Teledyne RD instruments workhorse ADCP operating principles 25

2.4 Errors in water velocity from ADCPs.. 26

2.5: Errors in salinity from SBEs and ISCATs 26

  2.5.1: Interpolating Salinity, Temperature, and Density... 28

2.6: Calculating Transport 29

2.7: Calculating Errors from the two different threshold measurements..................................... 31

3.1: ACC Parameters 33

  3.1.1: Transport, Salinity, and Temperature 33

  3.1.2: Width of the ACC.. 38

  3.1.3: Depth of the ACC 40

3.2: Wind in the Bering Strait and impacts on a buoyant coastal current.................................... 41

  3.2.1: Background on winds in the Bering Strait... 41

  3.2.2: Correlate wind to ADCP.. 43

3.3 Structure of the velocity field in the strait 43

  3.3.1: Correlation of the velocity mode with the wind 44

3.4: How does the theory of Buoyant Coastal Current (BCC) compare with observations?........ 45

3.5: Quantifying the impact of wind on the ACC.. 50

3.6: Separation of the ACC from the Alaskan coast due to southward wind 52

3.7 Frameworks specific for downwelling winds.. 61

3.8: Ekman dynamics across the entire eastern channel of the strait.. 65

3.9: Source of ACC waters? 67
3.10: Estimating ACC transport, freshwater transport, and heat only from A2 and A4 72
4.1: Summary 73
4.2: Future Work 75

List of Figures

Figure Number

1.1 Study area………………………………………………………………….. 6

1.2 Hydrographic section across the Bering Strait……………………………….. 9

1.3 Schematic of coastal current: (surface-trapped and slope-controlled)………. 13

1.4 Schematic of upwelling of isopycnals due to a southern wind forcing………. 17

1.5 Three wind regimes and their corresponding impacts on a buoyant current…. 19

1.6 Downwelling wind’s impact on a buoyant current…………………………… 21

2.7 Map of study area with moorings…………………………………………….. 23

2.8 Cross-section of the eastern Bering Strait with box method used for transport 31

3.9 Monthly averaged Bering Strait and Alaskan Coastal Current transport…….. 34

3.10 Time series of upper and lower layer salinity from moorings………………... 36

3.11 Time series of upper and lower layer temperature from moorings…………... 37

3.12 ACC width and presence from thermal wind and velocity shear calculations.. 40

3.13 Monthly averaged ACC depth………………………………………………... 41

3.14 Time series of meridional wind velocity from reanalysis data……………..… 42

3.15 1st mode of signal from SVD using meridional rotated velocity……………... 44

3.16 Contour plots of theoretical parameters using Lentz and Helfrich (2002)…… 46

3.17 Comparing observed/theoretical parameters using Lentz and Helfrich (2002). 49

3.18 Wind strength index contour plots using Whitney and Garvine (2005)……… 50

3.19 Wind required for reversal……………………………………………………. 53

3.20 Southward meridional wind events and ACC separation from coast………… 54

3.21 Three southward wind events (density) and ACC separation from coast……. 56

3.22 Three southward wind events (meridional velocity) and ACC separation from coast………………………………………………………………………… 57

3.23 Prediction of ACC separation from wind speed, duration, and $\Delta\rho$…………... 59

3.24 Contour plots of wind adjustment time from Whitney and Garvine (2005)…. 61

3.25 t_a from Moffat and Lentz (2012)…………………………………………….. 62

3.26 Schematic of wind’s impact on the Bering Strait during a northward wind event………………………………………………………………………… 65

3.27 ACC separation and flow reversal during a strong southward wind event…… 66
3.28 Ekman depth of northward wind events from Moffat and Lentz (2012)……… 67
3.29 Bering shelf water and salt budgets……………………………………………… 68
3.30 ACC freshwater transport correlated and shown with Yukon River discharge. 71
3.31 Comparing differences in transport calculations………………………………… 73

List of Tables

Table Number

2.1 Capabilities of mooring instruments…………………………………………..…. 24

2.2 Accuracies of mooring instruments……………………………………………. 25

2.3 Salinity correction by mooring and instrument type…………………………… 28

3.1 Correlation between wind and water velocity at each mooring…..…………….. 43

3.2 Correlation between wind and the modes of a SVD using water velocity……… 45

3.3 Details of southward wind events……………………………………………… 55

3.4 Details of northward wind events……………………………………………… 64

1.1 Characteristics of the Bering Strait Region

The Bering Strait is what remains of a land bridge that flooded approximately 14,400 years ago (*Elias et al.*, 1996). The Bering Strait lies between the Chukotka Peninsula (Russia) and the Seward Peninsula (Alaska, USA) (Figure 1). Relatively narrow and shallow (only 85 km wide and approximately 50 m deep), the Bering Strait is separated into two channels by the two Diomede Islands (*Coachman et al.*, 1975).

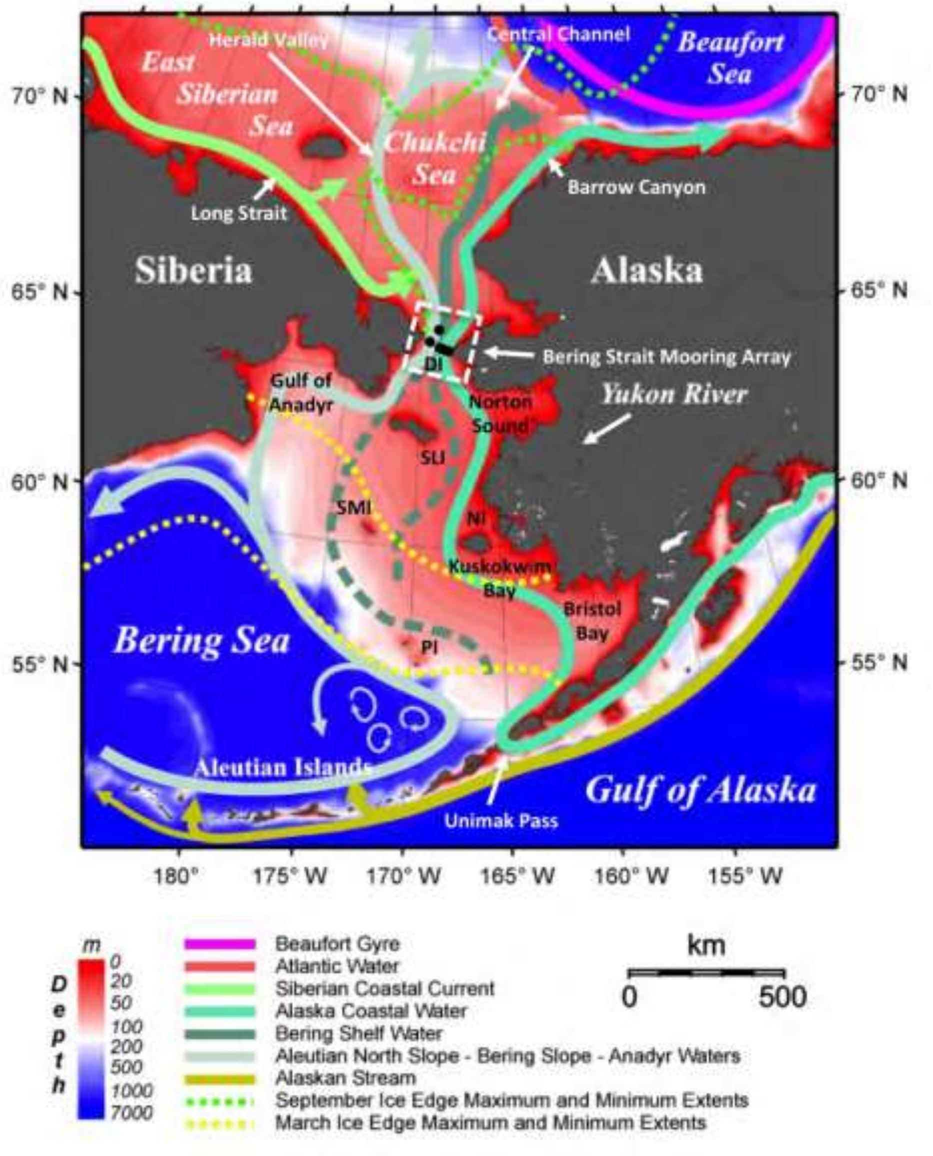

Figure 1.1: Larger view of study area as well as major currents in the region (taken from Danielson et al., 2011).

Prior work from year-round mooring measurements shows substantial seasonal variability in salinity, temperature, and transport in the Bering Strait, viz., 31.9 psu (December) to 33.0 psu (March) in salinity; -1.8ºC (January-April) to +2.3ºC (September) in temperature; and 0.4 Sv (January) to 1.3 Sv (June) in transport (monthly mean climatology from 1990 to 2004) (*Woodgate and Aagaard*, 2005). Under typical summer conditions (Figure 1.2), the Bering Strait water column is a two layer system, with cold, dense, saline water at depth and warmer, fresher water near the surface and down to approximately 10-20 m (generally in the eastern strait), with the western channel generally being saltier than the eastern channel (*Coachman et al.*, 1975; *Woodgate et al.*, 2015). Hourly variability during summer is much greater than monthly mean data. Hydrographic data from August 2010 in Figure 1.2 shows an example of how variable temperature and salinity can be in the strait at one time: temperatures from ~12ºC to colder than 2ºC, and salinities from 29 psu to 33 psu. In addition to the surface warm fresh layer typically ubiquitous in the strait in summer, still warmer and fresher waters are usually found in the upper part of the eastern side of the Bering Strait- this is the Alaskan Coastal Current (ACC) (*Woodgate et al.*, 2015), and the topic of this thesis. Salinity and temperature values for the waters of the ACC can be approximately >4ºC warmer and >3 psu fresher than the main Bering Strait throughflow (*Woodgate and Aagaard*, 2005). [1]

Contributing to the two-layer system discussed above are thought to be two things, 1) solar heating, and 2) water masses from different parts of the Bering Sea. There are two different water masses often considered as being present in the Bering Strait, namely the cold and salty Bering Sea Water (BSW), and the warm and fresh Alaskan Coastal Water (ACW) (*Coachman et al.*, 1975). Bering Sea Water is a combination of the slightly warmer and fresher Bering Shelf water, originating from the Bering Sea Shelf, south of the Bering Strait, and the slightly colder and saltier Anadyr Water (*Coachman et al.*, 1975), also coming from south of the strait, from the Gulf of Anadyr, northwest of the Bering Sea. Alaskan Coastal Water has, in the past, been generally defined as water with a temperature of 6-10 ºC and salinity of 30-31 psu (*Coachman et al.*, 1975) although more practically, ACW is perhaps better defined as the waters fresher than the main channel flow, since salinities in the Bering Strait varies widely depending on the season and year (*Coachman et al.*, 1975).

---

[1] Throughout this thesis, salinities will be cited on the Practical Salinity Scale, and labelled as such by the dimensionless unit psu.

The annual mean velocity in the Bering Strait is northward and about 30 cm/s, equivalent to approximately 0.8 Sv annual transport (*Woodgate et al.*, 2005). In the eastern Bering Strait, the Alaskan Coastal Current (ACC) can reach speeds of up to 150 cm/s during strong northward winds, and both the ACC and the mean flow can reverse during strong southward winds (*Woodgate et al.*, 2015; *Woodgate and Aagaard*, 2005). The tidal flow of the region is relatively small, with maximum velocities on order of about 5 cm/s (*Woodgate et al.*, 2005) and thus no tidal filtering has been performed for this thesis. Note the annual mean throughflow of the Bering Strait (northwards) is opposite in direction to the dominant wind direction, which is southward in the annual mean (*Woodgate et al.*, 2005).

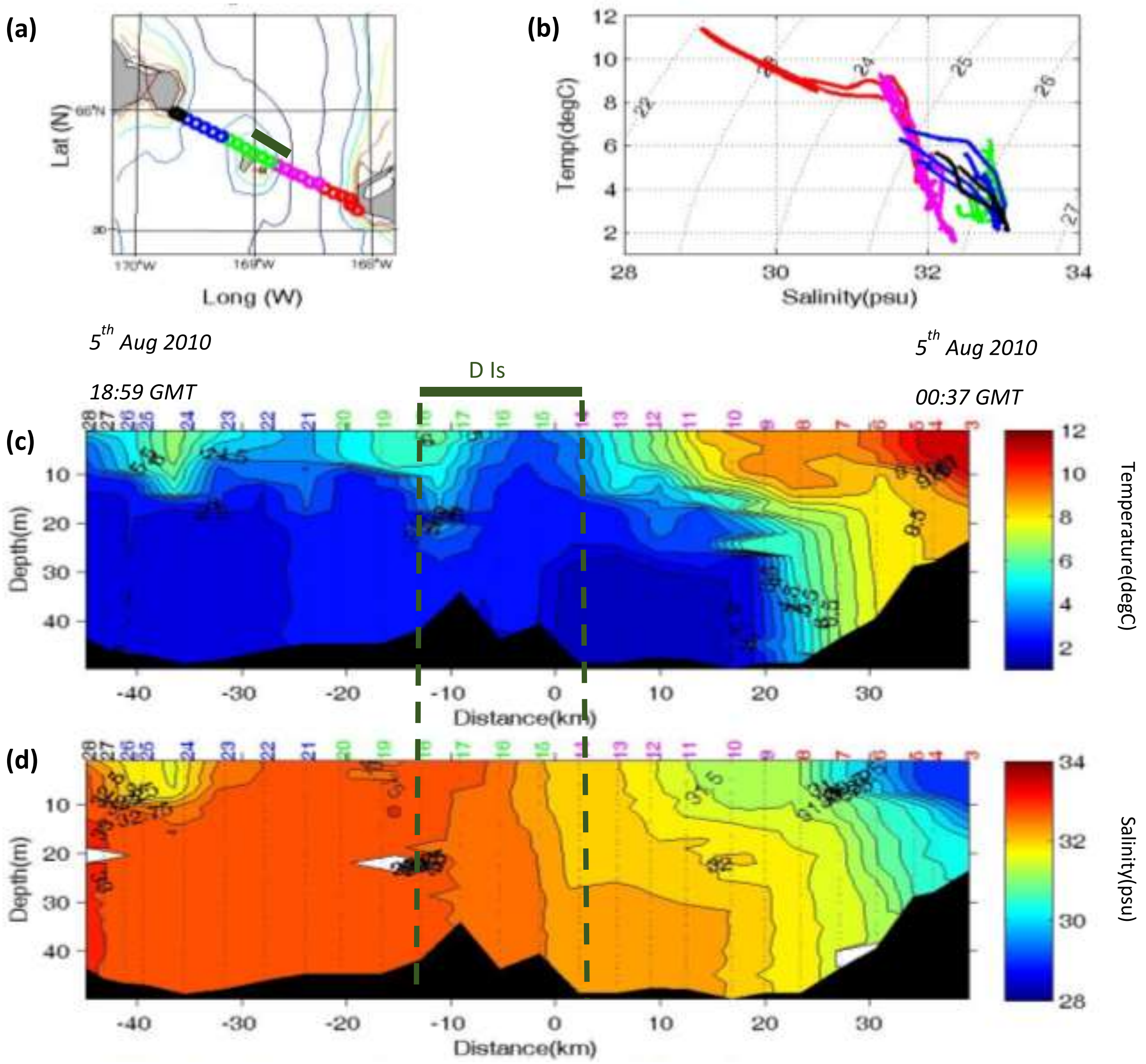

5th Aug 2010

18:59 GMT

5th Aug 2010

00:37 GMT

Figure 1.2: August 2010 hydrographic section across the Bering Strait taken from vessel Professor Khromov/Sprit of Enderby showing (a) map, (b) temperature-salinity distribution of the transect, (c) and sections of temperature (d) and salinity. Colors numbers above (c), (d), represent hydrographic stations. The brown bar above the sections indicates stations likely in the wake of the Diomede Islands. The dates at the top of the figure are for the start and end of the hydrographic section. Distances are measured from the west side of the U.S. channel. Reproduced from Woodgate et al. (2015).

The mean throughflow of the Bering Strait has been attributed to a pressure head difference between the Arctic Ocean and the Pacific Ocean (*Coachman and Aagaard*, 1966; *Stigebrandt*, 1984) modified by the local wind forcing (see *Woodgate et al.* (2005) for a discussion). Recent work attributes the variability in this pressure head term to changes in the Arctic via changes in sea level of the East Siberian Sea (ESS) (*Peralta-Ferriz and Woodgate*, 2017).

The Bering Strait has, at times, two seasonal currents, usually only present in summer months. One of these currents is the Siberian Coastal Current (SCC) (*Weingartner et al.*, 1999). The SCC flows southward along the Siberian Coast, and in some years also south along the western coast of the Chukchi Sea, but does not reach the Bering Strait every year. The SCC has been shown to reach the Bering Strait during strong southward wind conditions for short periods of time (between 1-10 days). The SCC often carries sea ice from the Arctic along the Russian coast before being deflected by the Bering Strait throughflow into the central Chukchi Sea. The SCC is forced by winds, Siberian river outflows, and ice melt, with an estimated average speed of 10 cm/s (*Weingartner et al.*, 1999).

The other seasonal current, the Alaskan Coastal Current, impacts the Bering Strait every year and is the main focus of this thesis. The first reports of the ACC in the scientific literature are from shipboard temperature and salinity measurements by *Paquette and Bourke* (1974), and later studies using satellite imagery by *Ahlnäs and Garrison* (1984). The ACC flows northwards along the west coast of Alaska, and is thought to originate primarily from freshwater river discharge from sources such as the Yukon River (discharge of ~200 km^3/yr) (*Aagaard et al.*, 2006). The Alaskan Coastal Current should not be confused with the *Alaska* Coastal Current, which is found along the southern side of the Aleutian Chain. Part of this current enters the Bering Sea through Unimak Pass in the Aleutian Islands (*Ahlnäs and Garrison*, 1984; *Woodgate and Aagaard*, 2005), and may in part contribute to the freshwaters of the ACC. The ACC is generally found to be present in the Bering Strait from April to December, as an approximately 10 km wide and 40 m deep current, and the core of the ACC is estimated to be approximately 3 psu fresher and 4ºC warmer than the ambient water of the strait (*Woodgate and Aagaard*, 2005).

Based on shipboard CTD/ADCP data, an estimate of instantaneous summer ACC transport is ~0.2 Sv, equivalent to a total freshwater transport of about 0.03 Sv relative to 34.8 psu, typically taken as the mean salinity of the Arctic Ocean (*Aagaard and Carmack*, 1989;

Woodgate and Aagaard, 2005). From mooring data spanning 1990-2004, an annual mean estimate of ACC transport is 0.08 ± 0.02 Sv, equivalent to a freshwater transport of approximately 0.007 to 0.014 Sv (*Woodgate and Aagaard*, 2005). From mooring data spanning 2003-2015, the annual mean transport of the ACC, estimated from mid-depth velocities at A4, are ~0.16 ± 0.01 Sv (*Woodgate*, 2018), compared to 0.15 Sv using annual mean 11m depth velocities at A4 from 2003 and 2004 (*Woodgate et al.*, 2006). Estimates of mean annual salinity for the ACC (from mooring and CTD data) are 30.3 ±0.5 psu, but during periods of strong flow in the summer, the instantaneous salinity can be as low as 29 psu (*Woodgate and Aagaard*, 2005). Wind forcing is an important factor for determining how this current will flow. Observations and idealized modeling suggest that southward winds can transpose the ACC off the Alaskan coast if strong enough (*Pisareva et al.*, 2015; *Woodgate et al.*, 2015), and this will be discussed in more detail later in the thesis.

1.2 Importance of understanding the Bering Strait for global circulation and climate change and solving real world problems

The Bering Strait throughflow has significant impacts on the heat and freshwater budgets of the Arctic Ocean (*Coachman et al.*, 1975; *Woodgate and Aagaard*, 2005; *Woodgate et al.*, 2010). From 2001 to 2007, calculations from mooring data suggest the Bering Strait northward oceanic heat flux significantly increased from 2-3 x 10^{20} J/yr in 2001 to a maximum of 5-6 x 10^{20} J/yr in 2007, enough energy to melt 1/3rd of the 2007 seasonal Arctic sea-ice loss area, assuming all of this heat's energy is directed at melting ice 1 meter thick (*Woodgate et al.*, 2010). Modeling studies suggest that the Bering Strait throughflow may influence global climate by increasing the freshwater input to the northern North Atlantic, hindering North Atlantic Deep Water (NADW) formation, and dampening the ocean's thermohaline circulation (*De Boer and Nof*, 2004; *Hasumi*, 2002; *Hu and Meehl*, 2005; *Huang and Schmitt*, 1993).

On December 1st, 2018, new shipping routes proposed by Russia and the United States and approved by the International Maritime Organization (IMO) went into effect for the Bering Strait. As sea ice decreases in the Arctic (*Nghiem et al.*, 2007) and shipping traffic increases, an oil spill due to a catastrophic shipping collision or grounding event becomes a more likely scenario. As discussed in the June 24th 2016 edition of the Alaska newspaper, the Nome Nugget, the closest oil spill response team is located in Anchorage, Alaska, with only two small shipping containers of hazardous material clean-up gear available in Nome. Thus, a spillage in the strait, in turn, would face long wait times for any major ship, cleaning equipment, and personnel (*Conservation et al.*, 2018; *Thomas and Conger*, 2016). Being able to better quantify the ACC can have direct implications for understanding how to deal with this disastrous situation.

Many fisheries biologists are interested in the flow of the ACC as it can have dramatic influences on the transport of fish larvae and therefore their successful reproduction (*Eisner et al.*, 2013).

The ability to accurately quantify the ACC will provide model validation and increase the predictive capability of oceanographic modelers for both regional, Arctic, and global modeling. This has direct impacts for governmental regulatory agencies and other scientists.

1.3 Theoretical framework for a Buoyant Coastal Current (BCC)

The ACC is essentially a buoyant coastal current and thus more likely shares theoretical features with other buoyant coastal currents. Initial work (1970s) on the behavior of a buoyant coastal current (also called a density current) showed with laboratory experiments that rotation inhibits the lateral spreading and mixing of a density current (*Saunders*, 1973; *Stern et al.*, 1982). All of this initial work considered currents against a vertical wall. However, this is likely a poor approximation to the real world, as most coastal currents flow against sloping, rather than vertical, topography. Indeed in the late 1980s to early 1990s, more experiments and numerical modeling studies showed that a sloping bottom had significant impacts on the dynamics of buoyant coastal currents (*Chao*, 1988), however no theoretical framework of these conclusions was derived. *Chapman and Lentz* (1994) were the first to provide some detailed theoretical insight for buoyant coastal currents. They looked specifically at how a uniformly sloping bottom impacts the ability of a current's density gradient to advect water offshore in a bottom boundary layer. They found that even with density anomalies as small as 0.1 kg/m^3, density advection in the bottom boundary layer dominated shelf circulation (*Chapman and Lentz*, 1994). Building on these results, *Yankovsky and Chapman* (1997) predicted the vertical structure and offshore spreading of a localized buoyant inflow (density current) onto a sloping continental shelf. They were able to parameterize the distance a plume can move offshore in relation to the inflow depth of freshwater, the density anomaly, the water inflow velocity, and Coriolis force. They also parameterized the depth at which the plume remains in contact with the bottom boundary (hereon referred to as the "foot" of the current) in relation to the inflow width, the inflow depth of freshwater, the density anomaly, the water inflow velocity, and the Coriolis force (*Yankovsky and Chapman*, 1997).

Following these other works, *Lentz and Helfrich* (2002) expanded the theoretical framework of buoyant coastal currents. They developed a scaling theory for buoyant gravity currents in a rotating reference frame on a sloping bottom. Similar to *Yankovsky and Chapman* (1997), the scaling theory uses known transport, the Coriolis parameter, the angle of the sloping bottom, and the density anomaly to define the structure (width and depth), nose (front edge of the current) speed, and propagation speed of a buoyant coastal current.

Lentz and Helfrich (2002) define two scenarios for gravity currents along a sloping bottom; slope-controlled and surface-trapped (Figure 1.3).

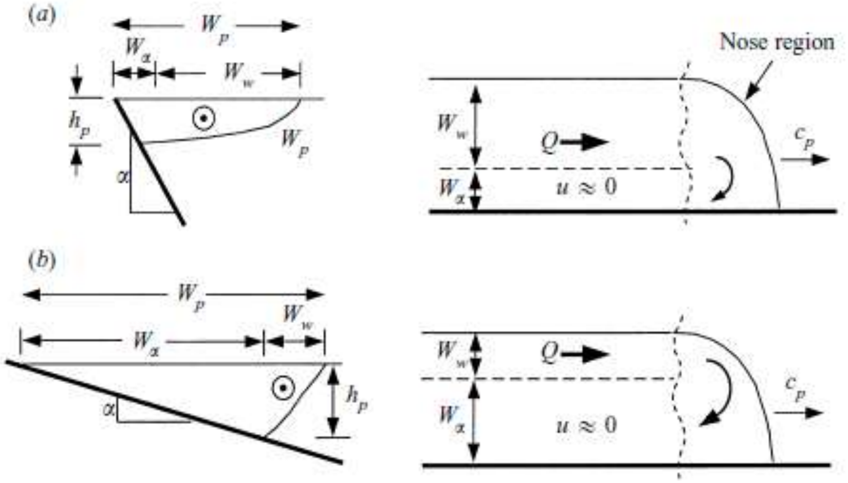

Figure 1.3: Reproduced from Lentz and Helfrich (2002). Schematic cross- sections (left) and plan view (right) of a buoyant gravity current geometry and circulation for (a) a surface-trapped and (b) a slope-controlled current. W_p *is the total width of the current,* W_α *is the offshore distance to the foot of the front,* W_w *is the width offshore of the foot of the front,* h_p *is the maximum thickness of the current (depth),* α *is the slope of the topography,* Q *is the transport,* u *is the speed of the inshore portion of the current, and* c_p *is the nose speed of the current.*

A **slope-controlled** gravity current is defined as a current that is in significant contact with the bottom slope such that bottom friction is an important component of the current's dynamics. For **slope-controlled** currents, along-slope flow onshore of the front's foot drives an offshore transport in the bottom Ekman layer which stretches and widens the gravity current.

One key assumption that Lentz and Helfrich make is that the bottom boundary layer advection continues until the velocity at the foot of the front is zero, and thus at this point the bottom boundary stress is zero. The second (alternative) regime identified is a **surface-trapped** gravity current. In this scenario, the current has much less contact with bottom topography. This is the default regime for gravity currents against a wall and is what all previous studies had been considering (*Lentz and Helfrich*, 2002).

A detailed scaling theory is developed to explain the dynamics of a gravity current over a sloping bottom and addresses the geometry (thickness and width) and propagation speed given transport, density anomaly, Coriolis parameter, and bottom slope values. The depth of these buoyant coastal currents (BCCs) is derived to be:

$$h_p = \sqrt{\frac{2Qf}{g'}} \tag{1.1}$$

where Q is the transport of the current, f is the Coriolis parameter $f = 2\Omega sin\theta$, where Ω is the rotational rate of the Earth (7.3x10^{-5} rad/s), θ is the latitude, and $g' = \frac{g(\rho_o - \rho_s)}{\rho_o}$ is the reduced gravity where g is gravitational acceleration, ρ_s is the density of the buoyant current and ρ_o is the density of the ambient water outside the current. This equation comes partially from *Yankovsky and Chapman* (1997) and the thermal wind equations:

$$\frac{\partial u_g}{\partial z} = \frac{g}{\rho_o f}\frac{\partial \rho}{\partial y} \qquad \frac{\partial v_g}{\partial z} = -\frac{g}{\rho_o f}\frac{\partial \rho}{\partial x} \tag{1.2}$$

which equate variations of velocity with depth to density, assuming geostrophy and the hydrostatic relationship.

In order to determine the propagation speed of a gravity current nose along a vertical wall (steep-bottom slope), *Lentz and Helfrich* (2002) begin with the phase speed of shallow water waves, using the reduced gravity parameter and h_p (bottom depth), i.e.,:

$$c_w = \sqrt{g' h_p} = (2Qg'f)^{\frac{1}{4}} \tag{1.3}$$

The authors then derive the propagation speed of a gravity current nose, c_α, in the limit of a small bottom slope through the relationship between density anomaly and the slope of the topography, viz:

$$c_\alpha = \frac{\alpha g'}{f} \tag{1. 4}$$

where α is the slope of the topography over which the current flows. The propagation speed of the nose of the current (c_p) is also derived:

$$c_p = \frac{c_w}{(1 + \frac{c_w}{c_\alpha})} \tag{1. 5}$$

This is always less than c_w. The authors also derive the width of various parts of the current (W_w, W_α, and W_p) (see Figure 1.3). W_w is the width offshore of the foot of the front, W_α is the offshore distance to the foot of the front, and W_p is the total width:

$$W_w = \frac{\sqrt{g' h_p}}{f} = \frac{c_w}{f} \tag{1. 6}$$

$$W_\alpha = \frac{h_p}{\alpha} = \frac{c_w}{f}\frac{c_w}{c_\alpha} \tag{1. 7}$$

$$W_p = W_w + W_\alpha = \frac{c_w}{f}\left(1 + \frac{c_w}{c_\alpha}\right) \tag{1. 8}$$

These equations allow us to calculate the total width of a buoyant coastal current given the density anomaly ($\Delta\rho$), the inflow velocity or transport (Q), the depth (h_p), and the Coriolis parameter (f).

In addition, *Lentz and Helfrich* (2002) derive a key non-dimensional parameter:

$$\frac{c_w}{c_\alpha} = \frac{(2Qf^5)^{\frac{1}{4}}}{\left(\alpha^4 g'^3\right)^{\frac{1}{4}}} \tag{1. 9}$$

This parameter is the ratio between the propagation speed of the gravity currents in the limit of steep bottom slopes and in the limit of small bottom slopes. It can thus be used to determine if the current is surface-trapped, or slope-controlled. If the current is slope-controlled, $\frac{c_w}{c_\alpha} \ll 1$, and the current is more affected by bottom topography and friction. If the current is surface-trapped, $\frac{c_w}{c_\alpha} \gg 1$, the current is mostly independent of bottom topography and behaves similarly to a current against a vertical wall. As a general rule, the slope-controlled limit will occur for currents with large transports at higher latitudes with smaller density anomalies and smaller bottom slopes (*Lentz and Helfrich*, 2002). We will discuss the parameter regimes relevant for the ACC in Chapter 3.

Another general finding is that slope-controlled currents have most of their transport incorporated in a thinner offshore region (Figure 1.3), with the onshore region of the current being generally quiescent, with negligible velocity. It is also important to note that (as shown above) the nose moves at a different speed to the main body of the current (the nose speed is slightly slower than the current's propagation speed because as the current moves along, water from the faster offshore region turns shoreward to fill in the onshore quiescent region).

1.4 Wind's influence on a Buoyant Coastal Current

The theory above is for a buoyant coastal current (BCC) with no other external forcing. In the Bering Strait, local wind forcing is clearly important. Thus, we consider also the theory of wind on a BCC. Much earlier than work done on buoyant coastal currents (BCCs), *Csanady* (1977) expands upon the simple geostrophic adjustment problem and develops equations to parameterize the wind forcing needed to upwell the thermocline of a water mass to the sea surface against a coast. This process can lead to separation of a BCC away from the coast. It is also important to note that once the current separates from the coast, it no longer follows the physics that control buoyant coastal currents. *Csanady* (1977) defines two parameters. The first, I, is the time-integral of the along shelf wind stress, viz:

$$I = \int_0^t \frac{\tau}{\rho} dt \qquad (1.\ 10)$$

where τ is the wind stress, ρ is the water density, and dt is the amount of time integrated over. The second:

$$C = \frac{h_t}{h_b}(h_t + h_b)fR_i \quad (1.\ 11)$$

represents the minimum impulse required for "full" upwelling, where "full" upwelling is defined as when the pycnocline is raised to the sea surface through Ekman transport (Figure 1.4). Here, $R_i = \frac{1}{f}\sqrt{\frac{g\varepsilon h_t h_b}{(h_t+h_b)}}$ is the internal Rossby radius of deformation for a two-layer fluid , where $\varepsilon = \frac{(\rho^b - \rho^t)}{\rho^b}$, g is gravity, $\rho^b$is the density of the bottom layer and $\rho^t$is the density of the top layer, $f$is the Coriolis parameter, h_t is the height of the top layer, and h_b is the height of the bottom layer (as per Figure 1.4).

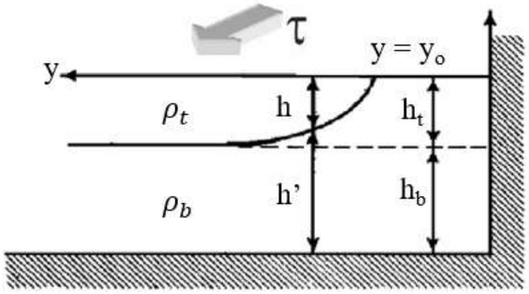

Figure 1.4: Reproduced from Csanady (1977). Schematic shows upwelling occurring in a two-layer fluid. When I is greater than C, the bottom layer's isopycnals are upwelled to intersect the surface. Note that C uses the internal Rossby radius for a two-layer fluid.

Whitney and Garvine (2005) extended this work by investigating the general influence of wind on a BCC. They found an upwelling wind tends not only to spread plume waters offshore through Ekman transport and also to mix the upper layers of the BCC. Downwelling winds also mix the upper layers of the water column but, in contrast to upwelling winds, have a tendency to narrow the BCC. *Whitney and Garvine* (2005) also developed a wind strength index (W_s), which estimates if a plume's along shelf flow is dominantly wind driven or buoyancy-driven:

$$W_s = \frac{u_{wind}}{u_{dis}} \quad (1.\ 12)$$

Here, u_{wind} is the wind-driven current velocity scale, i.e., $u_{wind} = \sqrt{\frac{\rho_{air}C_{10}}{\rho C_{Da}}}U$, ρ_{air} is the density of air, $C_{10}$is the surface drag coefficient, C_{Da} is the bottom friction coefficient, ρ is the water density, U is the along-shelf components of the wind, and u_{dis} is the buoyancy-driven current velocity where $u_{dis} = \frac{1}{K}(2g'Qf)^{\frac{1}{4}}$, where K is the Kelvin Number (dimensionless coastal current width) assumed to be 1, making u_{dis} identical to Equation (1.3) above. When W_s < 1, the current is considered to be buoyancy driven and when W_s > 1, the current is considered wind driven. The authors also derived a parameter that calculates the time it takes to tilt a plume's isopycnals such as to either shrink a current's width by half or spread it by half, depending if the wind is downwelling or upwelling (*Whitney and Garvine*, 2005):

$$t_{tilt} = \frac{KRh_1\rho f}{16|\tau_{sx}|} \tag{1. 13}$$

where $KR = L_1$ (L_1 is equivalent to half the width of the BCC), h_1 is the depth to the foot of the current (similar to h_p from Lentz and Helfrich (2002)), ρ is the density of the water, and $|\tau_{sx}|$ is the wind stress where $|\tau_{sx}| = \rho_{air}C_{10}|U|U$. Subsequently, *Lentz and Largier* (2006) studied how the Chesapeake Bay buoyant plume is impacted by wind and identified three regimes of a buoyant plume's response to wind forcing. These three regimes are shown schematically in Figure 1.5.

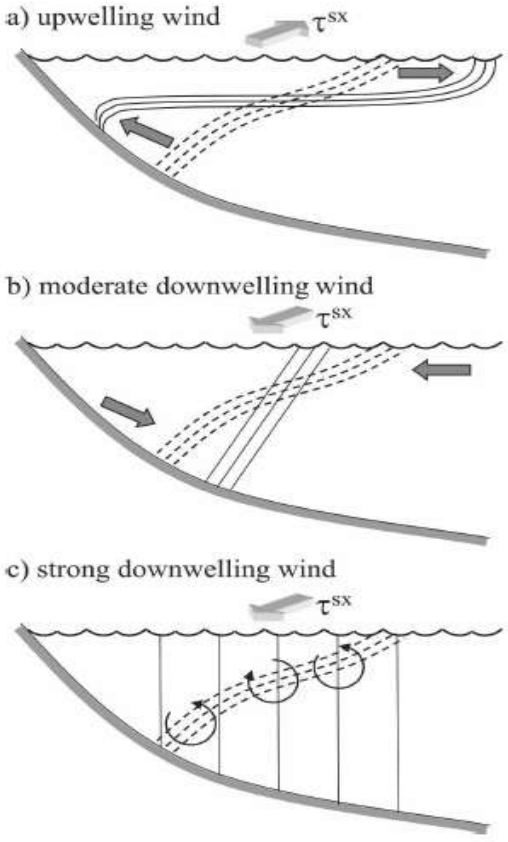

Figure 1.5: Reproduced from Lentz and Largier (2006). Schematic of buoyant plume response to different along-shelf wind forcing. (a) upwelling winds flatten the plume front, causing plume to thin and widen. (b) moderate downwelling winds steepen the front, causing plume to thicken and narrow. (c) strong downwelling winds force vertical mixing that widens the plume front, but does not cause much change in plume width, as the current is pushed against the coast and not spread across open water.

Lentz and Largier (2006) also identified wind stress values that fit into each of the three regimes. The **first regime was for weak upwelling winds** (wind speeds < 4 m/s for the Chesapeake Bay plume). Here, the buoyant coastal current becomes thin, as Ekman transport pushes the current away from the coast. The authors found from observations of the Chesapeake Bay plume that width is variable and does not have a clear dependence on wind stress, possibly because weak upwelling winds can easily affect small buoyant coastal currents. Currents under weak wind stresses eventually separate from the coast and move offshore where they tend to dissipate. The front slope is generally not steep. The **second regime was for moderate downwelling winds** (northwards in the case of the Bering Strait) (wind speeds between 4-7 m/s for the Chesapeake Bay plume). For this regime, wind-driven cross-shelf advection steepens the front of the current, causing the plume to narrow and thicken in depth due to onshore Ekman transport. The **third regime was for strong downwelling winds** (wind speeds > 7 m/s for the Chesapeake Bay plume). During strong downwelling winds, vertical mixing dominates the system, and isopycnals become nearly vertical, as the water column homogenizes, but the plume width does not significantly change.

The impacts of strong upwelling winds on BCCs were not studied by *Lentz and Largier* (2006) directly, as many previous studies had been done on qualitatively characterizing the effects. Previous studies showed that strong upwelling winds caused the current to separate from the coast, spread offshore, and disperse if winds are strong enough (*Fong and Geyer*, 2001; *Hallock and Marmorino*, 2002; *Hickey et al.*, 1998; *Johnson et al.*, 2003; *Johnson et al.*, 2001; *Rennie et al.*, 1999; *Sanders and Garvine*, 2001). A theoretical framework was then derived by *Lentz* (2004) describing the response of a BCC to upwelling favorable winds. Lentz (2004) derived buoyant plume characteristics as a function of time, given the wind stress, the characteristics of the buoyant plume prior to the wind forcing, and a critical value for the bulk Richardson number (assumed to be constant).

Finally, *Moffat and Lentz* (2012) derive a more detailed theoretical framework for the response of a buoyant coastal plume to *downwelling*-favorable wind stress. Their theory provides a resulting width, depth, density anomaly, and along-shelf transport of the plume (the equations are many and can be found in *Moffat and Lentz* (2012)). They find that downwelling wind stress can mix the plume waters and create cross-shelf circulation which can significantly deepen and narrow the current, depending if the current is “bottom-trapped” or “surface-trapped” (as described in *Lentz and Helfrich* (2002), see Figure 1.3). Bottom-trapped currents feel small changes from these downwelling winds, compared to surface-trapped plumes. They also develop a timescale (t_a) that estimates how long it would take for cross-shore Ekman circulation to steepen the isopycnals of the current which depend on the frontal slope of the current and the slope of the topography. Importantly, their theory starts with the assumption that the initial density field of the current contains constant vertical and lateral gradients which do not change significantly during the downwelling-favorable wind event (Figure 1.6). They discuss that this assumption may not be reasonable when comparing their theory to observations (*Moffat and Lentz*, 2012).

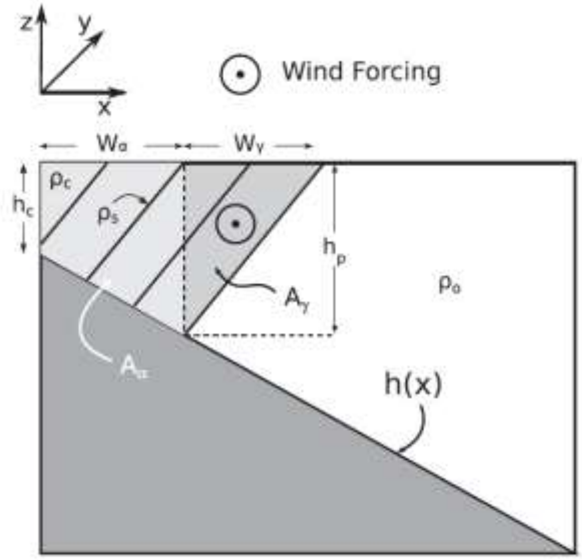

Figure 1.6: Schematic of initial plume geometry setup. Notice the constant vertical and lateral density gradient. The plume is initialized on a shelf with a vertical wall of depth h_c at the coast with a constant bottom slope and constant density, ρ_0. After the initial adjustment due to wind, the plume depth becomes h_p and the total plume width becomes $W_{p=}W_\gamma + W_\alpha$, with A_γ being the area of the frontal potion of the plume, and A_α is the area of the inshore portion of the front.

2.1: Introduction to moored data

In this chapter, we discuss the details of the seven-mooring array which contains the data used in this thesis. The Bering Strait was first measured using long-termed moored instrumentations in September 1990-1991 with the start of an initially joint program between the U.S. and the USSR, called the joint US-USSR Circulation Study of the Chukchi Sea. When this program ended in 1994, measurements ceased in Russian waters but continued in U.S. waters in a time series which has been almost unbroken until the present, with the exception of summer 1996 through summer 1997 (*Woodgate et al.*, 2015). In 2004, a National Oceanic and Atmospheric Administration (NOAA) led program, the Russian-American Long-term Census of the Arctic (RUSALCA), reinstated moorings in Russian waters in the Bering Strait, and this program continued until 2011 in collaboration with the US National Science Foundation (NSF) funded International Polar Year (IPY) and Arctic Observing Network (AON) programs. Since 2000, the mooring cruises which service the moorings also take CTD sections in the Bering Strait (US, or both US and Russian waters, depending on permissions from the State Department) and the southern Chukchi Sea. These CTD measurements provide an important calibration baseline for the mooring instruments. CTD data has allowed us to create a detailed 2-D section of the strait, allowing us to visualize the ACC in the eastern Bering Strait. This will be discussed more in depth in Section 2.5: Errors in salinity from SBEs and ISCATs.

2.2: Mooring array location and instrumentation

Moorings are typically in the water for approximately one year and are generally serviced during summer months, typically in July/August. Throughout the years, the number of moorings present in the strait has varied greatly, from as little as one mooring in 1995 to a maximum of eleven in 2011. Due to the large number of moorings deployed in 2011, we have chosen to focus on data from this 2011-2012 deployment season for this thesis. From east to west in the Bering Strait, the moorings we have taken into consideration are A5-11, A4-11, A4W-11, A2E-11, A2-11, A2W-11 (Figure 2.7). The last two digits of the mooring name indicate the year of deployment and the first two characters indicate the geographic location of the mooring. We also use data from the “climate site” A3-11, located approximately 35 km north of the other moorings, the site being so named because previous studies have shown that measurements from this site provide a useful average of the oceanographic properties of both the Bering Strait’s east and west channels (*Woodgate et al.*, 2015). The names of these moorings will be shortened to simply A5, A4, A4W, A2E, A2, A2W, and A3 for the duration of this thesis. 2011 was also the first and only year thus far that a mooring has been placed at sites A5 and A2E. The expectation of these extra moorings was that they would capture more detailed information on the seasonality of the ACC than the typical array (Figure 2.7).

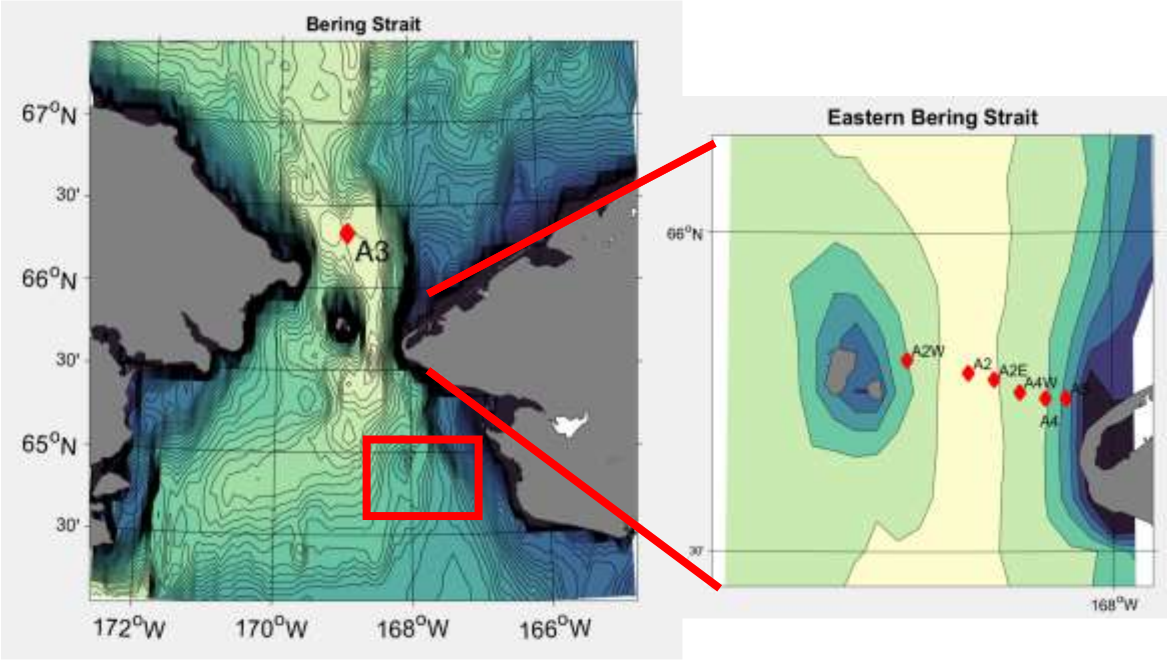

Figure 2.7: Map of moorings in the Bering Strait used for this thesis. The islands to the west are the Diomede Islands and the land on the right is the Alaskan coast. Note A3 located approximately 35km north of the Diomede Islands. Color contours are in 10m intervals.

All 2011 Bering Strait moorings measured temperature, salinity, and water velocity at one or more levels. Six of these seven moorings (all except A5) carried upward-looking Teledyne RD Instruments 300-kHz Acoustic Doppler Current Profilers (ADCPs). These same moorings also carried a near surface “ISCAT”, an instrument which measures upper water column temperature and salinity, designed by the University of Washington’s Applied Physics Laboratory (APL). These instruments sit in ice-resistant cages which help them survive impacts with ice keels during winter months (*Woodgate*, 2011). All moorings carried a near bottom (12m from the bottom) temperature and salinity recording instrument, either an SBE model 16 SEACAT or SBE model 37 MicroCAT built by Sea-Bird Electronics (SBE). One large difference in instrumentation for water velocity is that A5 used an Aanderaa Acoustic Recording Current Meter (RCM) with turbidity rather than an RDI ADCP. This means that the mooring at A5 was only able to record water velocities at one depth (39m), whereas the other moorings had ADCPs which could measure water velocities throughout the water column, nominally from just above the instrument (~43m) to the surface, although in practice, surface waves and reflections contaminate the upper ~10m. The tables below provides a summary of instrumentation deployed in 2011 (Table 2.2), as well as the manufacturers’ accuracies for each measured parameter.

Table 2.1: Location, serial number, data recording interval, instrument depth, water depth, and measured variables. Acronyms are as follows: NR=instrument not recovered, ND=no data, AARI= AARI Current meter, ADCP=RDI acoustic doppler current profiler, BPG= Seabird bottom pressure gauge, FLT=Wetlabs Biowiper fluorescence and turbidity recorder, ISCAT= near-surface Seabird temperature and salinity sensor in trawl resistant housing with near bottom data logger, ISUS=nutrient analyzer, RCM9= Aanderaa acoustics recording current meter, CRM9T= Aanderaa acoustic recording current meter with turbidity, pCO2= SAMI pCO2 sensor, pH= SAMI pH sensor.

Moorings	**Latitude (N) (WGS-84)**	**Longitude (W) (WGS-84)**	**Instruments**	**S/N**	**Recording Interval (min)**	**Instrument Depth (m)**	**Water Depth (m)**	**Measured Variables**
A2W-11	65 48.022	168 48.061	ISCAT	6964	NR	17	53	press, temp, cond, salt
			ISCAT Logger	2	30	N/A	53	N/A
			300kHz-ADCP	9396	30	44	53	various
			SBE16	1224	60	47	53	press, temp, cond, salt
			FLTUSBWetlabs	1261	N/A	47	53	flur, turb
			AURAL	129	N/A	47	53	marine mammal acoustics
			SBE26p-BPG	1135	30	51	53	press, temp
A2-11	65 46.866	168 34.069	ISCAT	5468	NR	18	56	press, temp, cond, salt
			ISCAT Logger	4	30	N/A	56	N/A
			300kHz-ADCP	2332	30	45	56	various
			SBE16woptics	4604	60	49	56	flur, turb
			ISUS	_017	N/A	49	56	nitrate
A2E-11	65 46.254	168 28.064	ISCAT	7111	NR	17	56	press, temp, cond, salt
			ISCAT Logger	6	30	N/A	56	N/A
			300kHz-ADCP	7967	30	47	56	various
			SBE37 Microcat	5826	15	47	56	press, temp, cond, salt
A4W-11	65 45.423	168 21.954	ISCAT	7112	NR	18	54	press, temp, cond, salt
			ISCAT Logger	3	30	N/A	54	N/A
			300kHz-ADCP	13756	ND	42	54	various
			SBE16	1698	60	45	54	press, temp, cond, salt
A4-11	65 44.762	168 15.770	ISCAT	5591	5	17	49	press, temp, cond, salt
			ISCAT Logger	1	30	N/A	49	N/A
			300kHz-ADCP	9397	30	38	49	various
			SBE16	1700	60	41	49	press, temp, cond, salt
			FLTUSBWetlabs	1260	N/A	41	49	flur, turb
			SBE26p-BPG	1134	30	47	49	press, temp
A5-11	65 44.397	168 11.081	RCM9T	1173	60	37	44	water velocity, turb
			SBE16	_0005	60	39	44	press, temp, cond, salt
A3-11	66 19.594	168 57.502	ISCAT	7110	30	15	57	press, temp, cond, salt
			ISCAT Logger	24	30	N/A	57	N/A
			300kHz-ADCP	7695	15	44	57	various
			SBE37 Microcat	5361	N/A	44	57	press, temp, cond, salt
			SAMI pH	P0029	N/A	46	57	inorganic carbon chemistry
			SAMI pCO2	16	N/A	46	57	inorganic carbon chemistry
			SeaPhOx	N/A	N/A	46	57	inorganic carbon chemistry
			AanderaaOx	1488	N/A	46	57	inorganic carbon chemistry
			SBE37 Microcat	7156	N/A	46	57	press, temp, cond, salt
			SBE16woptics	4639	60	48	57	press, temp, cond, salt
			ISUS	124	N/A	48	57	nitrate
			AURAL	130	N/A	50	57	marine mammal acoustics

Table 2.2: Accuracies of mooring instruments. The lower value is the manufacturer's calibrations, while the higher value is the results after our calibration of the instruments.

Accuracies	**ISCAT**	**SBE (16 & 37)**	**ADCP**	**RCM**
Pressure	*1(dbar)*	*1 (dbar)*	*N/A*	*N/A*
Temperature	*0.02 (°C)*	*0.02 (°C)*	*0.4 (°C)*	*0.05 (°C)*
Salinity	*0.02-0.1 (psu)*	*0.02-0.1 (psu)*	*N/A*	*0.2 (psu)*
Velocity	N/A	N/A	*0.5-1 (cm/s)*	*2 (cm/s)*
Heading	N/A	N/A	*1-6.6 (°)*	5 (°)

2.3: Teledyne RD instruments workhorse ADCP operating principles

The ADCPs used in this study are Teledyne RD Instruments 300-kHz broadband Workhorse Sentinel ADCPs. Each ADCP has four circular transducer faces which are arranged at a 20° angle from the vertical axis of the instrument (*Teledyne*, 2011). The data collected from the four sonar beams allows the ADCP to estimate three velocity components (eastward, northward, and vertical) and make an estimate of the uncertainty in these estimates. These velocity components are estimated from the doppler shift of a sound signal ("ping") reflected off small particles in the water column called sound scatterers (e.g. plankton, sediment). It is important to note that a key assumption in these calculations is that these sound scatterers are all moving at the same velocity as the water. From these three components, the profiler can also calculate an error velocity, which is a measure of how homogenous the water column velocity is and how stable the velocity is over the time period of data averaging (the "ensemble", here usually ~27 minutes). A large error velocity can be due to malfunctioning equipment, inhomogeneities in the water column in space or time, or particles in the water column that are not moving at the same velocity as the water (e.g. fish, or parts of the mooring) (*Teledyne*, 2011).

The ADCPs measure the velocity by splitting the water column into different bins, or sections. For our data, each bin was 2 m in height and the first bin was approximately 4 m from the head of the transducer. A4 had 18 total bins, A2E had 22 total bins, and the other three moorings (A3, A2W, and A2) all had 21 bins. Not all these bins return good data (discussed in Section 2.4 Errors in water velocity from ADCPs The ADCPs took 115 pings per ensemble, pinging every 14 seconds over a ~27-minute period, followed by a ~3-minute break to allow for other acoustic instruments on the mooring to record without interruption. This results in velocity data being recorded every 30 minutes, and the data may be considered as the 30-minute velocity average.

2.4 Errors in water velocity from ADCPs

As just mentioned, the ADCP data from the 300kHz RDI Acoustic Doppler Current Profilers was collected in 2 m bins. We discarded data from two regions, viz where ADCP bins contained large errors due to 1) interactions with mooring hardware equipment (e.g., the ISCATS or the mountings for the ISCATS) and 2) noise from surface scattering due to surface waves. The errors associated with noise in velocity near the surface are caused by turbulent mixing due to wave action.

As explained above, the ADCP measured error in relation to water column homogeneity. The following quality control tests were performed on the ADCP records in order to account for data error. Our first step to processing the ADCP data was to find data points whose error (estimated by the ADCP) was greater than 5 cm/s. For short clusters on these points (e.g., 6 or less points, equivalent to a data gap of 6 hours or less), we replaced these points with a linear interpolation in time between the good data points on either side. This generally removed spikes from the dataset known to be associated with equipment error. If there were more than 6 consecutive bad points (i.e., a data gap of more than 3 hours), we decided to leave the "bad data", as interpolating between this large gap of data would most likely introduce more error than was already in the data. After this had been completed, we considered the depth profile of the record-averaged data. This step helped us identify which bins we suspected had been contaminated by the hardware above the ADCP on each given mooring. Typically, we found that the bins at the same depth level as the ISCATs had errors that were much higher than the rest of the bins (and velocities lower than the adjacent bins), and thus we discarded the ISCAT level bins as well. Finally, we did not use bins that, over the whole deployment, had an average error of greater than 1 cm/s and a fraction of "bad" points (points that had error of greater than 5 cm/s) greater than 5%. This situation occurred primarily near the surface.

2.5: Errors in salinity from SBEs and ISCATs

Real data is "messy". This was obvious especially in salinity data from the SBEs and ISCATs where we identified strange coherent dips and spikes, as well as other more subtle issues. We considered two types of salinity errors. The first was short term spikes in salinity that lasted anywhere from hours to days, which could be due to, for example, some blockage in the conductivity cell. The second type of error was a longer term “drift” in the ability of an instrument to measure salinity accurately.

For the first type of error, large spikes over shorter amounts of time (~ 2-3 hours), we interpolated between the points we believed to be correct on either side of the salinity spike.

For the same type of spikes that occurred during winter, we took advantage of the fact that the water column should be at the freezing point during this time (as is found in past observations). This meant that we could use the salinity and pressure values recorded by the instrument to calculate an expected freezing temperature due to these recorded values. If this calculated freezing temperature was above the measured temperature, it indicated the salinity data measured contained errors. In order to fix this, we worked backwards from our recorded temperature values and, assuming the temperature of freezing, calculated the corresponding salinity value.

For the second type of salinity errors, instrument drifts over long periods of time, we analyzed data when the measured temperature was less than -1.75 ºC (very close to the known freezing temperature of water). These are times when we expect the water column to be homogenous. We then compared the salinity of the ISCAT (the higher instrument) to the SBE (the lower instrument) to check for density inversions in the water column, which was attributed to the SBE drifting too fresh (previous work with these mooring instruments has shown they do not drift salty). Most SBE instrument errors (e.g., biofouling, or scouring of the salinity cell by sediment) result in erroneous freshening. When these density inversions were identified, we used the trend line to correct the salinity values (see Table 2.3).

All the errors that were corrected were due to the instruments drifting fresher throughout the year. These drifts in salinity could have been due to many issues. One issue could have been that the instrument was not treated properly for biofouling before use. Fine grain sediment from the water column could have been another culprit, which may have scoured out the instrument inside the device that measures conductivity, changing the salinity measurements over time. The third, and most common error, is that, despite anti-biofouling measures, some amount of biofouling was still able to grow within the cell. Each of these factors would make the measurements drift fresh.

Another way to validate these drifts over the entire length of our record was to compare the mooring measurements with a pre-recovery CTD cast. These CTD casts were conducted before recovery of the moorings. However, as for safety reasons, the CTD casts were not exactly on the mooring location (up to 500m away). The mooring instruments are only recording temperature and salinity hourly, and thus the CTD cast could be up to half an hour away from the mooring sample data. These CTD casts served as a less stringent validation check on the errors that had been previously calculated.

Once the moorings with salinity drifts were identified, an appropriate correction was determined. This correction was applied by ramping the salinity values of the mooring over the entire record, thus assuming the error increases linearly in time. This may or may not be a good assumption, however we have no information to elucidate this. Table 2.3 provides a list of the moorings which were corrected for salinity.

Table 2.3: Salinity corrections by mooring and instrument type. All data was ramped over the entire data record of approximately one year.

Salinity correction to the SBEs		Salinity correction to the ISCATs	
A3	Ramped by 0.2 PSU	A2W	Ramped by 0.1 PSU
A2E	Ramped by 0.3 PSU		
A4	Ramped by 0.3 PSU		
A5	Ramped by 0.2 PSU		

2.5.1: Interpolating Salinity, Temperature, and Density

In order to more usefully portray our salinity data in the cross section plots we use, we have artificially added temperature and salinity data from the SBE at A5 to the same mooring at 20 m depth. We have justified this because we suspect the water above the SBE (where the artificial ISCAT has been placed at 20 m) is at least as fresh, as warm, and as dense as the lower instrument. This artificial instrument ensures more reasonable numerical interpolations for visualization purposes.

2.6: Calculating Transport

One focus of this thesis is understanding the transport of the ACC and its contribution to the total flow through the Bering Strait. We calculated transport in the eastern Bering Strait (EBS) using just the ADCP data. The RCM data at A5 (near the Alaskan coast) mentioned in Table 2.2 is not included in this analysis because it only provides velocity data at one depth, unlike the ADCP data. Another reason A5 is not included is because we expect high levels of velocity shear in that location, which can be much more accurately provided by the neighboring ADCP at A4.

There are many methods by which one might estimate total transport from the mooring array, however we take the simplest approach, a more complex interpolation is not justified by the sparse data coverage we have. Ship's ADCP sections, and high correlations between flow at the various moorings indicate that, away from the region of the ACC, the flow field in the strait is largely homogenous, and thus that linear interpolation between moorings is a reasonable assumption. Practically, we divide the vertical east/west section of the eastern Bering Strait into boxes, each box containing one bin of velocity data from our ADCPs in the vertical and reaching horizontally to the mid-point between the two moorings (*Figure 2.8*). We justify this linear interpolation between moorings because previous work in the strait has shown the moorings are highly correlated (*Woodgate and Aagaard*, 2005). For the box edge near the coasts, we have assumed a vertical wall, at the distance equivalent to the 25m isobath (see Figure 2.8). The bathymetry data used in Figure 2.8 was obtained from a Nobeltek Chart of the region (version SDUS09RMAP13.dbr). It is important to note that our boxes do not cover the entire EBS and some of our boxes overlap land. One of the largest areas of water that are not covered by our boxes are the shallow waters near the Alaskan coast, which we estimate has a cross sectional area of ~42,680 m^2, which is only 2.5% of the box total. The other portions of land that are covered by boxes and the water that are not covered are relatively equal. As we only have four moorings and therefore four longitudes represented across the eastern strait, a distance of approximately 37 km, we decided this box geometry was the simplest for calculation purposes. We justify this because a majority of the eastern Bering Strait water not accounted for is water close to shore. From known buoyant coastal current theory and CTD measurements, we know that the water close to shore is typically quiescent and therefore would not contribute much to the overall transport calculations.

Five different transport values were calculated.

The **first** transport calculated was the entire transport of the eastern Bering Strait (called "**EBS**"). This was done by multiplying all the velocities measured by the ADCPs by the cross-sectional area of the corresponding box.

The **second** transport calculated was transport of just the ACC (called "**ACC**"). For this we needed to identify which boxes lie within the ACC. This was done by comparing each velocity (averaged over one day) of all the ADCPs to the velocity at the deepest bin of A2W. In other words, we are assuming that the bottom bin of A2W is a reasonable proxy for the background (i.e., non-ACC) Bering Strait throughflow. Any bin with a velocity greater than the bottom bin of A2W by a certain threshold was assumed to be in the ACC. To test the sensitivity of this method, we considered two separate thresholds, 5 cm/s and 10 cm/s (we will refer to these as "5 threshold error" and "10 threshold error" in the next section). These threshold values for transport are eventually combined into one value and the errors are calculated as described below in Section 2.8. The transport was then calculated by multiplying those boxes that surpassed the threshold by their cross-sectional area.

The **third** transport calculated was the excess transport from the ACC over the background flow (called "**ACCext**"). Here ACC boxes were identified as above, but now the transport was calculated using box area and box velocity minus the background throughflow (measured as the velocity at the bottom bin of A2W).

The **fourth** transport was the Bering Strait throughflow neglecting the ACC. This was calculated by multiplying a deep velocity bin from A3 by the known cross-sectional area of the Bering Strait in that location (4.25 km^2)) (*Woodgate*, 2018). We call this "**A3trans**".

The **fifth** transport calculated was the total Bering Strait throughflow (called "**Total**"). This was done by adding A3trans and ACCext.

The geographical line of the moorings we used in our analysis that span across the eastern Bering Strait (A2W, A2, A2E, and A4) does not run due east-west, but instead lie on a heading of approximate 103^o, while the average principal component of our ADCP data is 8.3^o. To calculate transport perpendicular to 90^o, but also taking into account the average principal component of our data, we used trigonometry to multiply our distances by cos(4.7^o) (103-90^o= 13^o-8.3^o=4.7^o).

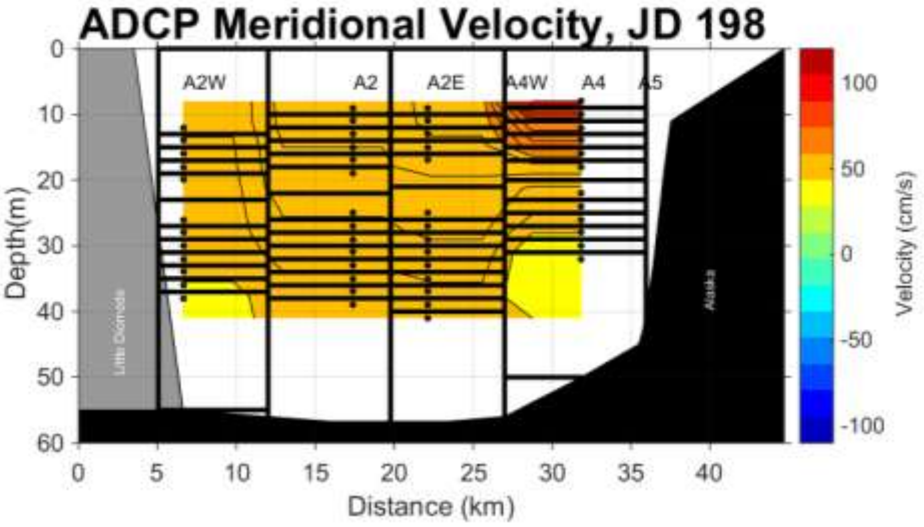

Figure 2.8: An example of a cross-section of the eastern Bering Strait looking northward. The black contours represent the topography used for our study. The east side is the Alaskan coast, and the west side is the Little Diomede Island in the center of the Bering Strait. The black boxes were used to calculate transport.

2.7: Calculating Errors from the two different threshold measurements

To avoid continual referencing two transport measurements from the two thresholds mentioned in Section 2.7, for this thesis, we have combined the 2 threshold estimates into one value and estimated the combined uncertainty in this value by combining 1) summing error in quadrature and 2) by taking the mean of the two measurements and finding the difference from the mean to the original measurements. For example, when calculating the monthly mean for each transport thresholds, each error was calculated by Equation (2.1):

$$error_5 = \frac{standard\ deviation}{\sqrt{number\ of\ effective\ degrees\ of\ freedom}} \tag{2.14}$$

Where $error_5$ is the error from the 5 threshold, and $error_{10}$ would be the error from the 10 threshold. Once we have this $error_5$ and $error_{10}$, we sum the two errors in quadrature:

$$error_t = \sqrt{\left(\frac{error_5}{2}\right)^2 + \left(\frac{error_{10}}{2}\right)^2} \tag{2.15}$$

Where $error_t$ is the error for the threshold values. Next, we found the absolute value between the two threshold measurements to the mean of the two data sets:

$$error_m = \frac{|thresh_5 - thresh_{10}|}{2} \tag{2.16}$$

where $thresh_5$ is the original transport value calculated with a threshold of 5 cm/s, and $thresh_{10}$ is the original transport value calculated with a threshold of 10 cm/s. Once we had $error_m$ and $error_t$, we summed them in quadrature to determine our final error:

$$error_f = \sqrt{\left(\frac{error_m}{2}\right)^2 + \left(\frac{error_t}{2}\right)^2} \tag{2.17}$$

When we refer to transport values, or any parameter that is calculated with transport values, the error associated with the value has been calculated in the above way.

3.1: ACC Parameters

3.1.1: Transport, Salinity, and Temperature

Transport

Though the Bering Strait is known to have high annual variability (*Woodgate et al.*, 2015; *Woodgate*, 2018; *Woodgate and Aagaard*, 2005), this thesis will not be considering interannual variability. Therefore, the data is from a single year starting July 15th, 2011 ending July 9th 2012.

A key question regarding the ACC is how much transport it contributes to the total Bering Strait throughflow. To assess this, we use the techniques described in Chapter 2 to calculate a) the total eastern channel transport ("EBS") as calculated from all the moorings with ADCPs (A4, A2E, A2, A2W) b) the total ACC transport ("ACC") as estimated from all moorings, identified by velocity greater than a certain threshold above the background flow (taken as the deepest A2W velocity) c) the contribution of the ACC which exceeds the background flow ("ACCext"), d) the traditional estimate of the total Bering Strait throughflow quantified from A3 alone, which neglects the ACC ("A3trans"). Thus, our new best estimate of the total Bering Strait throughflow is A3trans + ACCext = "Total". We consider the monthly means of these results for the deployment year considered here, from July 2011 and 2012, but we note that only August 2011 to June 2012 have complete data, and thus the results from July shall be taken with caution.

Our results show August 2011 has the highest monthly averaged ACC transport; 0.44 Sv (± 0.06 Sv), which is ~29% of the total Bering Strait throughflow. In this month, the standard A3 estimation of the throughflow (1.36 ± 0.15 Sv) is ~0.18 ± 0.02 Sv too low, as it neglects the contribution of the throughflow provided by the ACC (ACCext). Despite the ACC having the highest transport in August 2011, the highest total Bering Strait throughflow is in July 2012 (1.71 ± 0.11 Sv). There is actually no compelling reason to require that the ACC flow would peak when the total throughflow peaks. For example, the strongest meridional winds might be at a time when the ACC was absent.

We can also compare the ACC to the flow in just the eastern channel of the strait during summer months (July-October 2011 and May-July 2012). Here we find the ACC makes up the most (67%) of the eastern Bering Strait during September 2011. We also note that during earlier summer months (May and June 2012), the ACC contribution is less (33%). This emphasizes the point that the ACC is not as strong in May and June 2012 (early summer months) as it is in July and August 2011 (late summer months).

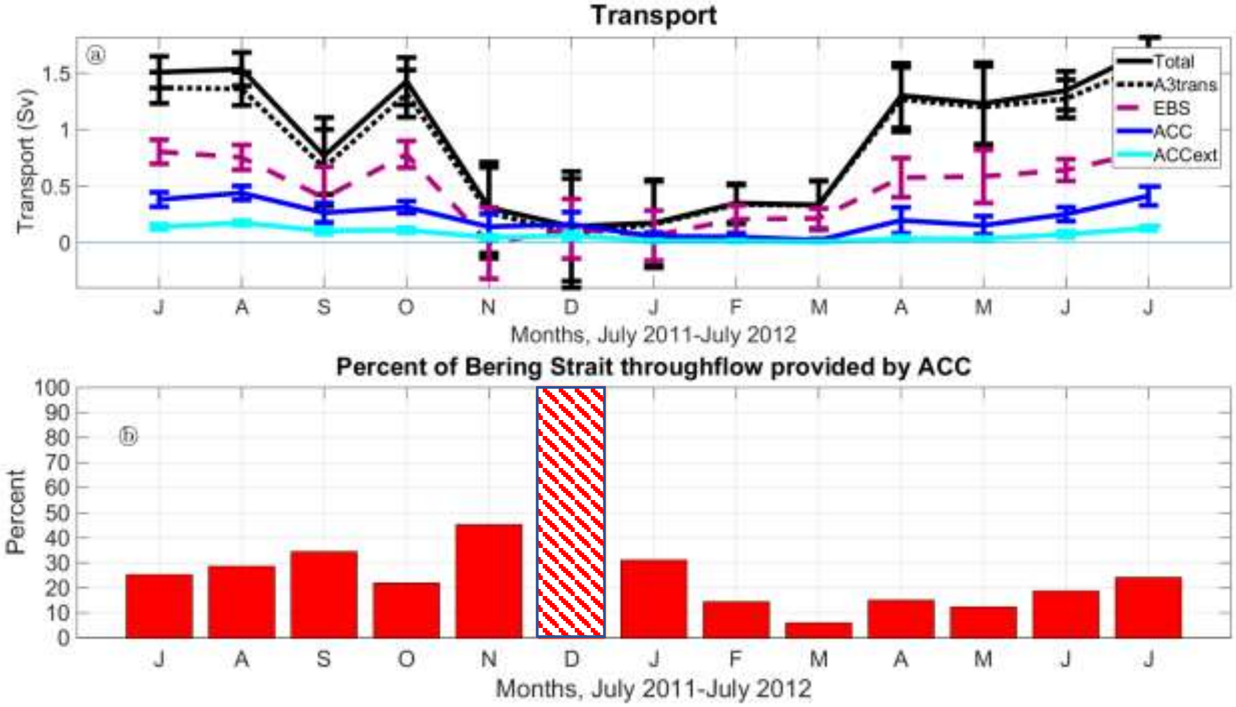

Figure 3.9: (a) Monthly averaged transport (in Sv) during our study year with error bars of total Bering Strait transport (Total, black), Bering Strait transport as estimated from A3 plus the missing contribution due to the buoyancy forced ACC (A3trans, dashed black), eastern Bering Strait transport including the ACC (EBS, purple dashed), total ACC transport (ACC, blue), ACC transport minus the background flow (ACCext, cyan) (b) The percent of the total Bering Strait throughflow provided by the ACC for each month. December is hatched because it artificially shows the ACC representing 100% of the Bering Strait throughflow. When the strong flow of the ACC is present in December (only for a short period of time) and it becomes averaged with the mean flow of the Total of that month (almost zero), it artificially represents most of that month's Bering Strait throughflow.

Salinity

As previously mentioned, the ACC is a seasonal current- with seasonal cycles of volume, temperature, and salinity. The freshest salinities are recorded in summer months, as well as the greatest differences in salinity across the eastern Bering Strait. The largest salinity difference recorded for the eastern Bering Strait is on August 15th 2011 at ~4.4 psu between the upper salinity measurement at A4 (a proxy for the ACC) and the lower salinity measurement at A2W (a proxy for the properties of the Bering Strait throughflow) (for accuracies of salinity measurements, refer to Chapter 2). The lowest salinity recorded in our record is not in the Bering Strait proper, but at the climate site (A3). This value was recorded on August 7th, 2011 at 25.8 psu by the upper instrument at A3. This salinity measurement is approximately 3 psu lower than any other salinity measurement recorded during our study, and ~1 psu lower than the other moorings on that day. We suspect this low spike in salinity may have been due to an intrusion by the Siberian Coastal Current, which is much more likely to reach A3, as it is located 35 km north of the Bering Strait proper. The lowest salinity recorded in the Bering Strait proper during our study was 28.3 psu by the upper instrument at A4, most likely within the ACC on August 9th 2011, 6 days before the largest salinity difference across the strait was recorded.

From the beginning of December to April, all instruments show a salinity increase by ~1.5-2 psu. The highest salinity value recorded is on April 10th, 2012 from A4 at 34.3 psu. This salinity increase in winter and subsequent decrease corresponds well with the formation of sea ice. Through ice data collected from our moorings in the strait during this time, we know A2W experienced ice as early as November 26th 2011 with ice last recorded on May 27th 2012. The highest monthly averaged sea ice thickness is during April, and the average thickness at this time was 2.8 m. Through conservation of salinity and mass, we are able to solve for a salinity change that this amount of ice formation would cause in the underlying water using Equation (3.18):

$$\Delta s = \frac{(\rho_i d_i)(s_0 - s_i)}{(\rho_0 h_0) - (\rho_i d_i)} \tag{3.18}$$

where ρ_i is the density of the ice (920 kg/m^3), ρ_0 is the density of water (both before and after the ice has formed- strictly these are slightly different, but the effect is small), s_0 is the salinity of the water before ice formation (31.5 psu), s_i is the salinity of the ice (6 psu), h_0 is the depth of the water column (50 m), and d_i is the thickness of the ice (2.8 m). This shows that if 2.8 m of ice were to grow on a 50 m water column, one might expect a ~1.4 psu increase in salinity due to brine rejection from the sea ice. Thus, the 1.5-2 psu salinity change observed from early autumn to the maximum monthly averaged ice thickness in April 2012 might easily be the result of ice formation, either in the strait or nearby. While it may be tempting to equate the decrease in river input in winter to the increased salinity, this is probably not the case. We would expect to see an increase in salinity more so at A4 than A2W if decreased river input were the cause of the increased salinity, however we see the entire strait increases in salinity at the same time at a constant rate.

Once the ice begins to melt in April 2012, the salinity of the Bering Strait begins to decrease to pre-winter salinity levels.

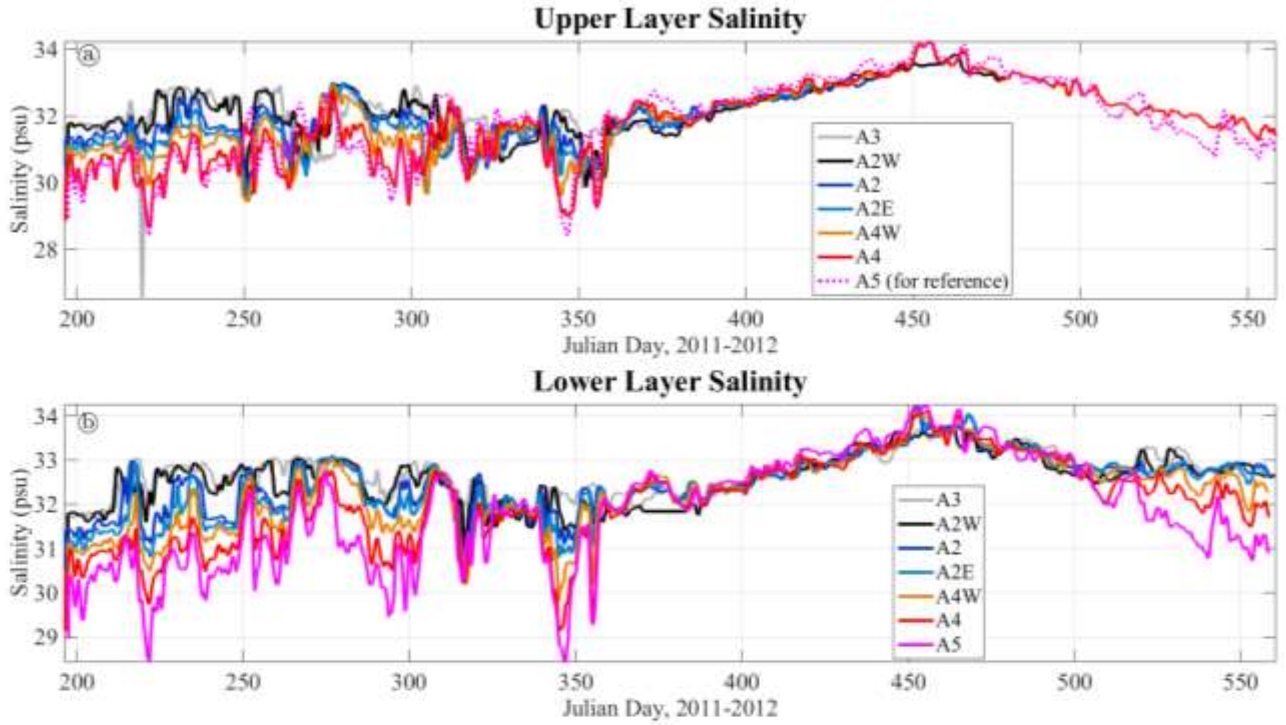

Figure 3.10: (a) Upper layer salinity measurements from each mooring in the study. The colors represent the moorings (see the legends). Note the A5 lower layer measurement is included for reference purposes (A5 does not include a measurement in the upper layer). The upper layer instrument sits at ~18m and the lower layer ~49m, depending on the mooring. Data has been daily smoothed using a boxcar filter. Time is in Julian days starting January 1st, 2011, thus data

shown are from July 2011 (Julian day 198) to July 2012 (Julian day 556). (b) Same as (a) but for the lower layer.

Temperature:

The temperature profile of the strait also has a strong seasonal pattern. The warmest temperatures as well as largest temperature differences across the eastern Bering Strait are recorded during the summer months. The warmest temperature recorded was from A5 (where only lower layer data are available), ~9.6ºC on August 9th, 2011. The largest temperature difference across the strait (~7.3ºC) occurred on July 27th, 2011 between the lower measurements at A2W and A5. By the end of October, the temperatures in the strait become relatively homogeneous and by mid-November, all the temperatures in the strait are at the freezing temperature (~ -1.8C) until mid-May when the spring warming takes place and the ACC arrives in the strait.

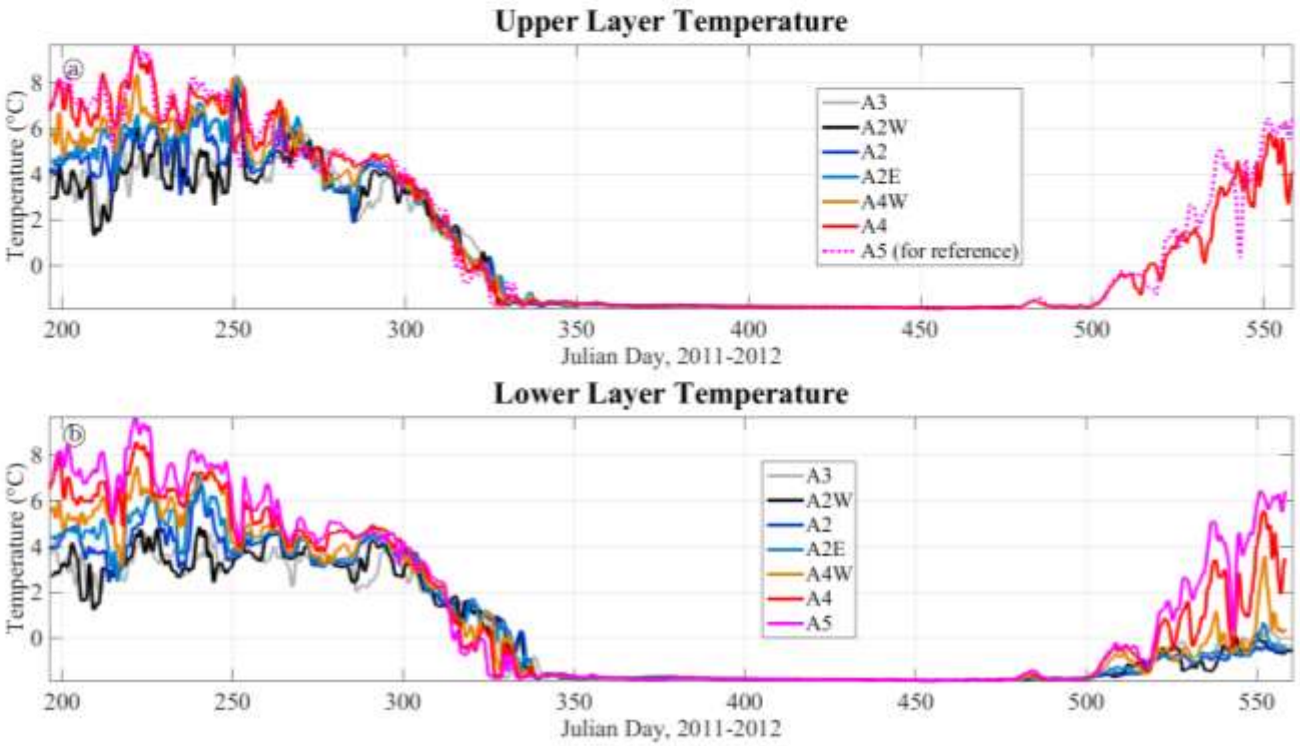

Figure 3.11: (a) Upper layer temperature measurements from each mooring in the study. The colors represent the moorings (see the legends). Note the A5 lower layer measurement is included for reference purposes (A5 does not include a measurement in the upper layer). The upper layer instrument sits at ~18m and the lower layer ~49m, depending on the mooring. Data

has been daily smoothed. Time is in Julian days starting January 1^{st}*, 2011, thus data shown are from July 2011 (Julian day 198) to July 2012 (Julian day 556). (b) Same as (a) but for the lower layer.*

3.1.2: Width of the ACC

The width of the ACC is an important parameter to be able to quantify, not only for physical oceanography purposes but also for understanding biological processes, such as the transport of fish larvae (*Eisner et al.*, 2013). Previous work has suggested (from CTD sections) that the ACC is typically 10 km wide (~ the local Rossby radius) (*Woodgate and Aagaard*, 2005). An obvious question is if we can find a better estimate of the ACC width from our sparse mooring data? A first guess would be to assume the "thermal wind" balance (i.e., that velocity shear is the result of horizontal density gradients) and use mooring based estimates of the velocity shear and the density difference across the strait to estimate the current width, viz:

$$\Delta x = \frac{-g\ \Delta z\ \Delta\rho}{\rho_0\ f\ \Delta v} \tag{3.19}$$

where $\Delta\rho$ is the density difference between the ACC plume and ambient waters, estimated as the density difference between the upper instrument from A4, the best estimate of ACC waters, and the lower instrument at A2W, the best estimate of non-ACC waters; Δv is the difference between the uppermost good ADCP velocity bin from A4 (~ 8 m depth) and the deepest good ADCP velocity bin from A2W (the best estimate of non-ACC flow), Δz is the depth between the two measurements at each mooring (~29 m), f is the Coriolis force, ρ_0 is the water density (taken as 1025 kg/m^3), g is gravitational acceleration, and Δx is the width of the current, assuming the current is up against a vertical wall. The result of this calculation is given in Figure 3.12, where we have masked values where $\Delta v < 20$ cm/s and $\Delta\rho < 0.5$ kg/m^3.

The annual average of these thermal width calculations yields an estimate of the annual mean ACC width of ~23 km, which is not close to the ~10 km of the Rossby radius, with the ACC widths ranging from 3.4-30.2 km. From these results, we conclude that using the thermal wind equations to estimate current width is not accurate.

We can use velocity shear at the moorings to give an independent estimate of ACC presence. If the shear between the uppermost and lowest good ADCP bin was greater than 20 cm/s at a mooring, we decided the ACC was present at that mooring (Figure 3.4). This gives a lower bound on the ACC width. As we only have three longitudes across the strait to look at shear, this leaves us with a crude estimate of ACC width, which has other substantial drawbacks e.g., if the current is deep enough to reach the deeper water velocity bin we used to calculate the lower level of shear, the shear between the top and bottom of the instruments would most likely not be above 20 cm/s. This could lead to an erroneous suggestion that the current was not present at that mooring. We conclude that using velocity shear at each mooring to estimate current width will not always provide an accurate representation of the current's width due to the large separation between moorings.

Another way we have to verify this width measurement is from CTD sections. Only one CTD overlaps our mooring data. These CTD data suggest an ACC width of 12.3 km on 16 July 2011. This is in agreement with the velocity shear method, which suggests the ACC is between A4 (10.3 km) and A2E (18 km). The thermal wind calculation during this time does not give an estimate of width because the velocity difference between the deepest good bin of A2W and the uppermost good bin of A4 is not more than 20 cm/s. Thus, we conclude, as above, that the thermal wind calculation is not an accurate method of estimating the ACC width. In contrast, the shear method may be accurate, but it only gives a very crude measure of the current.

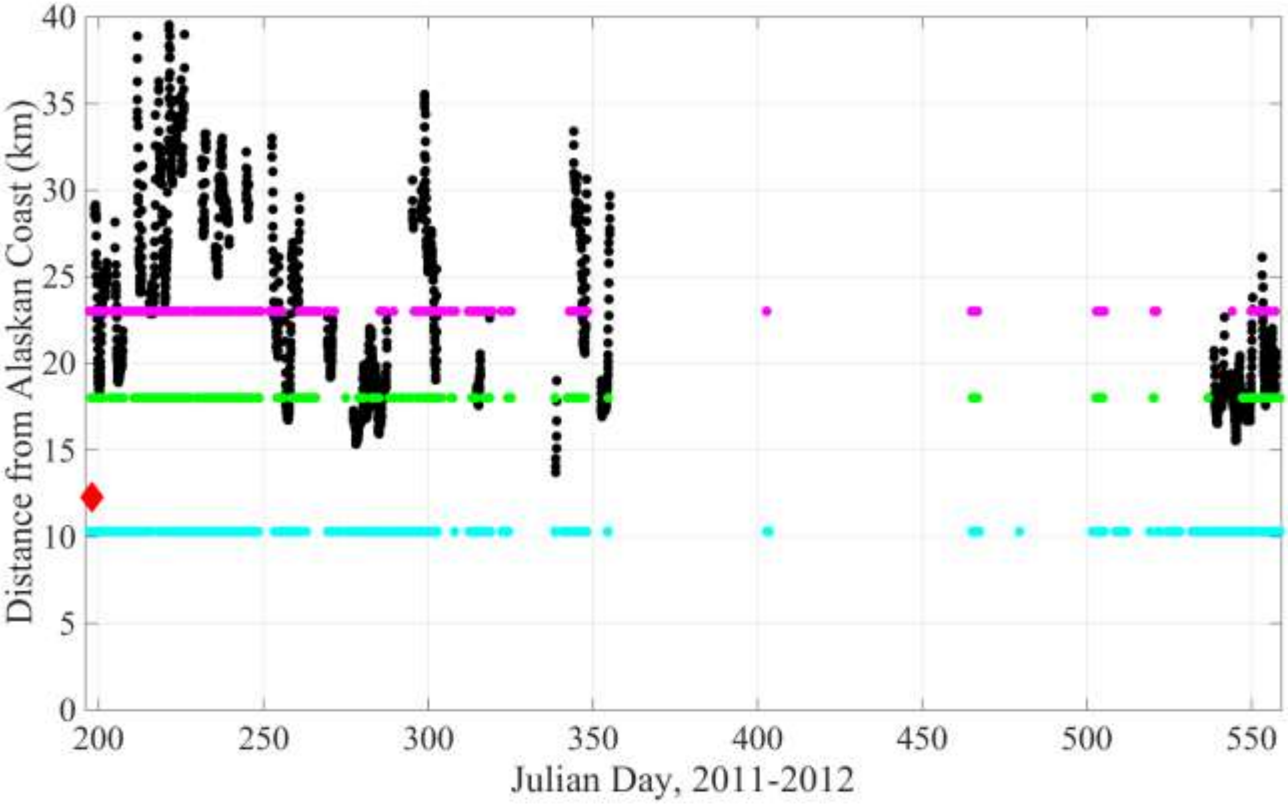

Figure 3.12: Estimates of ACC width in black from thermal wind equation (Equation (3.19)) for $\Delta\rho$ *values > 0.5 kg/*m^3*. The colored dots show times at each mooring when the water column shear at that mooring was > 20 cm/s, most likely meaning the current is at least as wide as the mooring (measured from the Alaskan coast). The y axis represents the ACC width, as measured from the Alaskan coast to the mooring. Cyan dots represent A4 (~10.3 km), green dots A2E (~18 km), and magenta dots A2 (~23 km). The red diamond is the only actual measurement of current width we have, estimated from the CTD section taken from the cruise on July 16th 2011.*

3.1.3: Depth of the ACC

Another key parameter of a buoyant coastal current is its depth. It is important to determine if the current is in contact with the ocean floor, as that has implications for its velocity and width. The depth of the ACC was calculated by using the water velocity shear thresholds previously mentioned in Section 2.6. The lowest bin depth that was greater than the deepest good bin of A2W by the threshold (5 or 10 cm/s) was labeled the ACC.

This analysis shows a strongly seasonal variability to the monthly averaged current depth. The monthly average was determined by averaging the depth for each day of the month then averaging over the entire month. From July 2011-October 2011, the monthly average current depth is 30 ± 10m. From May 2012-July 2012, the monthly average current depth is 24 ± 10m (Figure 3.13). As the ACC starts to weaken in November, the depth of the ACC shallows significantly from October. This is the opposite process to that which occurs in May when the ACC strengthens in the strait. During the winter, the ACC is not present, and therefore the depth is zero. Theoretical depths can be calculated given the transport and a density difference between the ACC plume and the ambient waters of the strait. This will be discussed below in Section 3.4.

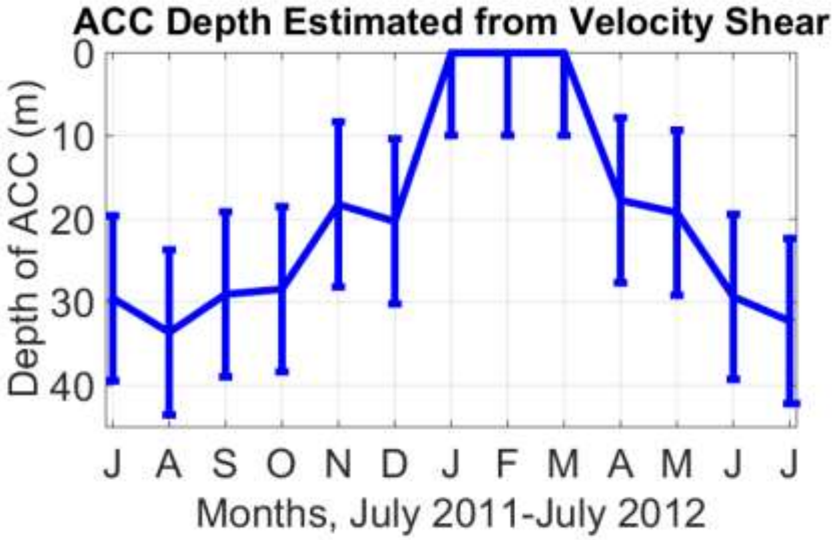

Figure 3.13: Observed monthly averaged depth of the ACC inferred from velocity shear.

3.2: Wind in the Bering Strait and impacts on a buoyant coastal current

3.2.1: Background on winds in the Bering Strait

The winds in the region of the Bering Strait are seasonal, and are driven mainly by the position of the Siberian and Beaufort high-pressure systems and the Aleutian low-pressure systems (*Aagaard et al.*, 1985). During winter, the Aleutian low penetrates far to the north of its typical position (near the Aleutian Islands), and its isobars become more closely spaced and become aligned approximately north-south. This alignment generates strong southward winds, with an average long-term speed of ~5 m/s. During the summer, when transports through the strait are high, winds are weaker (*Aagaard et al.*, 1985; *Danielson et al.*, 2014).

The wind data we use in this study are 6-hourly reanalysis data from the NCEP (National Centers for Environmental Predictions) (Figure 3.14). As we will show later in the thesis, wind is an important factor to consider in the Bering Strait, as it has a large impact on the current's parameters. During our study, 69% of the time the wind had a southward component with an average wind velocity during those periods of 6 m/s. The range of wind speeds during our study is anywhere from 0-37 m/s, with maximum northward and southward wind velocities ranging from 21 m/s to -17 m/s, respectively. During the summer of 2011 into late autumn, i.e., when the ACC is present, the average wind direction is southward 59% of the time, less often than the entire data record, with an average wind speed of 5 m/s southward. Winds during our study are rarely constant, with large storms occurring often (~8 strong events with meridional wind velocities over 15 m/s). The winds during the winter months are rarely northward, except during strong storms. In contrast, winds during the summer months are much more variable in direction, with the wind oscillating between northward and southward.

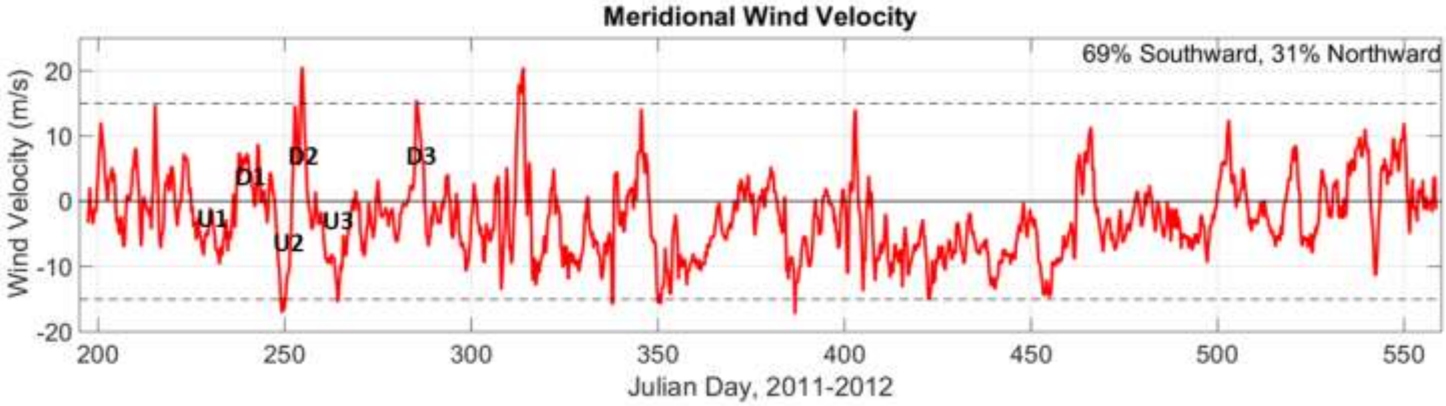

Figure 3.14: Northward wind velocity during our study. These data are from the National Centers for Environmental Predictions (NCEP) for location 65N, 170W. The numbers at top right show the percent of time the wind was northward and southward during the study. The light blue reference lines mark 15 m/s northward and southward wind velocities. The black labels represent naming conventions of wind events consistent with Tables 3.3 and 3.4.

3.2.2: Correlate wind to ADCP

The high correlation (r ~0.8) between meridional wind (or near meridional wind) and water velocity has been long known (*Aagaard et al.*, 1985; *Roach et al.*, 1995; *Woodgate et al.*, 2005).

In our data, we also found the meridional velocity of the wind to be highly correlated with the rotated meridional velocity of the ADCP data (r~ 0.69 for all moorings (*Table 3.4*.1)), with the highest correlation occurring at A4 (r = 0.7) (recall, we are using the velocity in the direction of the principal component of the ADCP data, 8.3º, Section 2.6).

Table 3.4: Correlating the meridional velocity of the wind to the meridional rotated velocity of the ADCPs at each mooring. Correlations significant above the 95% level ($p \leq 0.05$).

	A2W	A2	A2E	A4	A3	**Average**
Correlation Coefficient (r)	0.69	0.69	0.69	0.70	0.71	**0.70**

3.3 Structure of the velocity field in the strait

To investigate the structure of velocity in the strait, we performed a singular value decomposition (SVD) on the north/south and east/west velocities of the ADCP data set, i.e., good data from A2W, A2, A2E, and A4. The SVD was performed on three different rotations of the data set. The first rotation was the original meridional and zonal velocity data. For the second rotation, we considered the velocities parallel and perpendicular to the average principal component of the four moorings (8.3º). For the third rotation, we used the velocities parallel and perpendicular to the principal component of each mooring bin. The principal component of each bin was itself determined through a singular value decomposition analysis. The results from each rotation looked similar, with the first mode of the SVD representing approximately 59% of the variability of the data, while the second and third modes represented 7% and 5%, respectively- and are likely not significant. Thus, for brevity, we will focus here only on the results from the second rotation (i.e., rotated about the average principal component of all four moorings, 8.3º), and we will refer to these data henceforth as rotated velocity.

Figure 3.15 shows the spatial variability of the first mode (the first Empirical Orthogonal Function, EOF). Here, you can see what looks like a surface trapped current, indicative of the seasonally present ACC, pushed against the Alaskan coast, with velocities decreasing with depth and distance away from the coast.

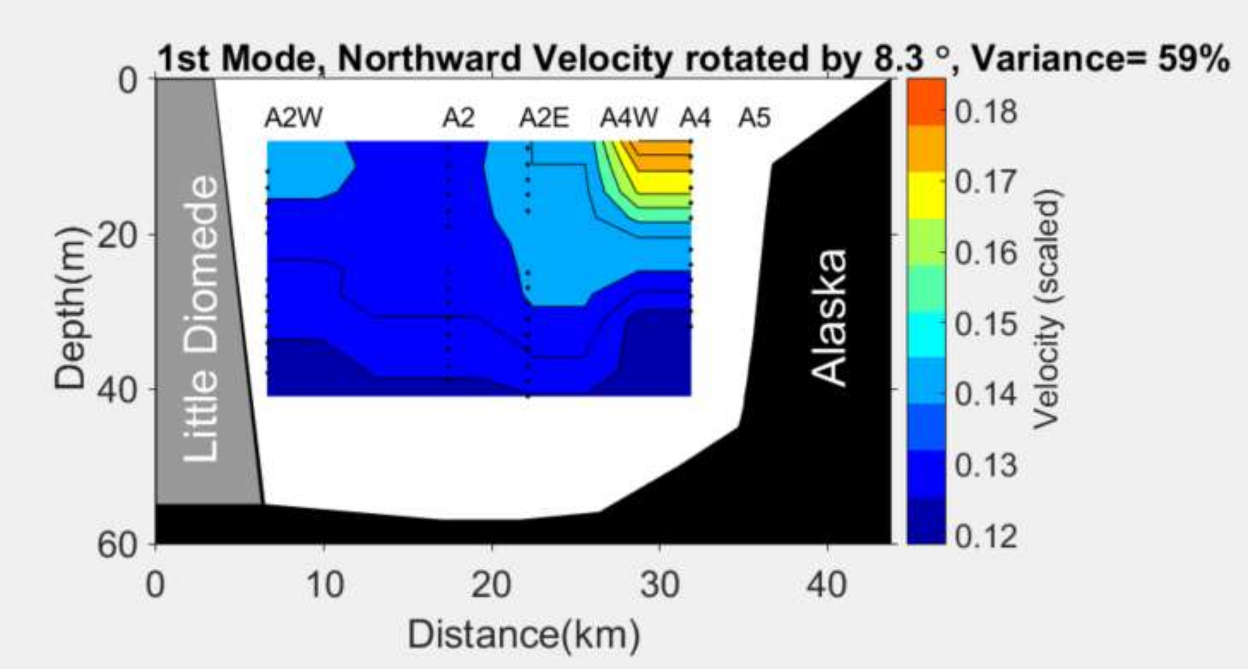

Figure 3.15: Cross section of the eastern Bering Strait with the 1st mode from a singular value decomposition (SVD) using meridional water velocity rotated to 8.3º. 59% of the variance of the data are captured by this first mode, with subsequent modes representing far less (~7%, ~5%, respectively). Notice the strong presence of the surface-trapped ACC-like feature along the Alaskan coast.

3.3.1: Correlation of the velocity mode with the wind

Given the high correlation of velocity with local wind, and the high portion of the variance explained by the first EOF, it is not perhaps surprising that we find also the meridional component of the wind is highly correlated to the first mode of the 8.3º rotated ADCP data (Table 3.5). This shows not only is the main channel flow strongly influenced by the wind, but also the entire structure of the flow (with the ACC) has a strong relationship to the local wind forcing.

Table 3.5: Correlation coefficients from the first three modes of ADCP rotated data to the meridional wind component. r^2 *shows the amount of variability of each mode explained by the wind relationship. All correlations are significant above the 95% level* ($p \leq 0.05$).

Modes of EOF	Correlation Coefficients (r)	r^2 (Variability)
1	0.71	50%
2	0.12	1%
3	0.13	2%

3.4: How does the theory of Buoyant Coastal Current (BCC) compare with observations?

Using the theory mentioned in Chapter 1 from *Lentz and Helfrich* (2002), we were able to calculate theoretical values that we could compare with observations. Using a set latitude (θ=65.7º) for our study area to calculate the Coriolis force, we calculated theoretical values of a current width, depth, and speed with the input variables of transport and a density anomaly (Figure 3.16). We were also able to determine theoretical values of the “critical parameter” (Equation 1.9). Recall that when the critical parameter is much less than 1, the current is considered to be surface-trapped, when the critical parameter is much greater than 1, the current is considered to be slope-controlled.

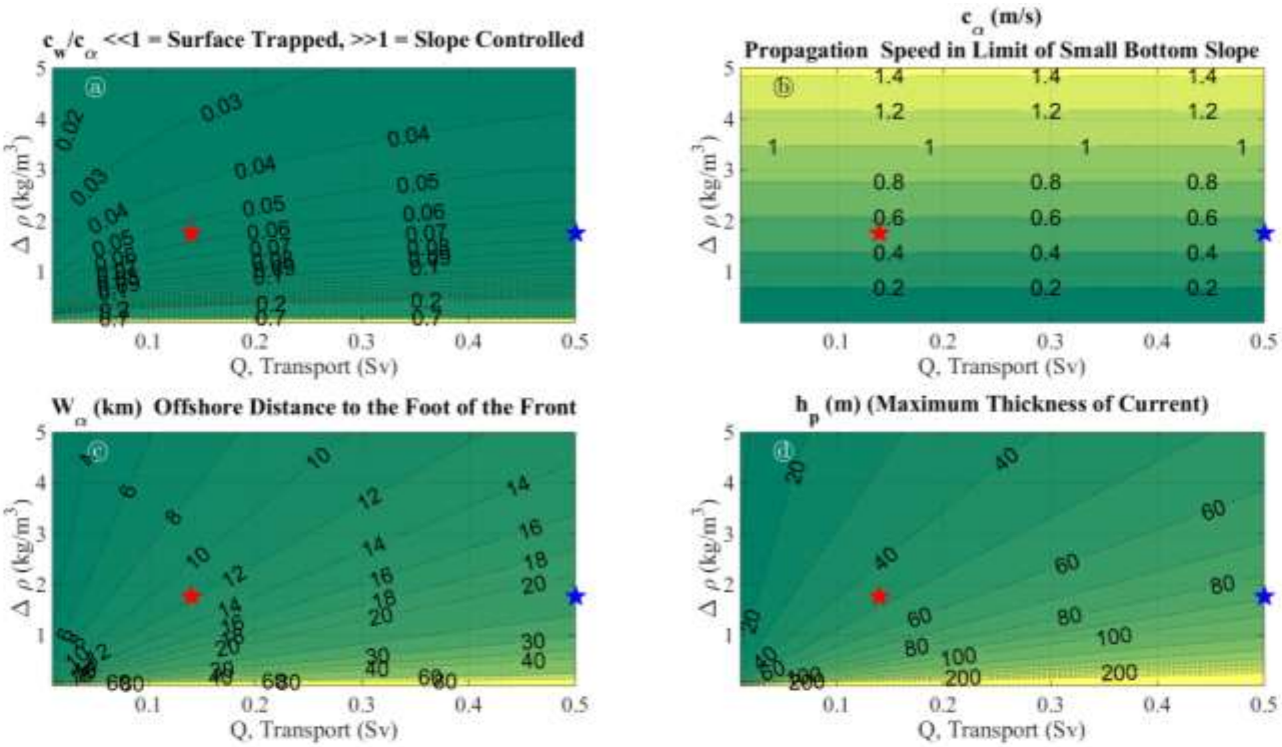

Figure 3.16: Contour plots of theoretical parameters from Lentz and Helfrich (2002). The starts represent the daily average condition on July 17th 2011 during the CTD cast collected in the Bering Strait for that year. The red stars represent the transport that is due solely to the buoyancy forced velocity (ACCext), while the blue stars represent the total transport of the ACC (ACC). (a) Critical-parameter described by Equation 1.9. When $\frac{c_w}{c_\alpha} \ll 1$ *the plume is surface trapped. When* $\frac{c_w}{c_\alpha} \gg 1$ *the plume is slope-controlled. (b) Propagation speed of a buoyant coastal current in the limit of a small bottom slope. (c)* W_α *, the offshore distance to the foot of the front of the buoyant coastal current. (d)* h_p*, the maximum thickness of the buoyant coastal current (depth). All of the y axis are density anomaly and the x axis are transport. The ranges shown are all possible ranges of the ACC from monthly averages.*

The colored stars on Figure 3.16 represent the daily average condition in the strait during July 17th 2011, during one of two CTD sections we have for the strait. The two different stars represent our different quantifications of the ACC (blue= ACC, red= ACCext). The CTD section from July 17th 2011 suggest the ACC was mostly surface-trapped, with a depth of ~42m at the foot of the front, and an offshore distance to the foot of the front of ~12km. At this time, the average meridional velocity of A4 at 8 m depth was ~93 cm/s.

The theoretical parameters we calculate require the inputs of transport, which is measured as discussed in Section 2.6, and $\Delta\rho$ which we quantify as the difference in density between the lower instrument at A2W and the upper instrument at A4. Given these inputs, the theoretical parameters show the ACC should be surface trapped, with a propagation speed of ~50 cm/s, both of which are observed in our CTD cast. However, because we have quantified the ACC transport in two different ways (ACC and ACCext) we have two different values for both the width (W_α) and depth (h_p) of the current. Using the ACC variable (total ACC transport) we calculate a width (W_α) of ~22 km and a depth (h_p) of 90 m, both of which are much greater than observations (Figure 3.16). Using the ACCext variable (ACC transport minus the background flow at the bottom of A2W) we find a width (W_α) of ~12 km and a depth (h_p) of ~47 m, both which agree very well with observations. The hypothesized reason why ACCext is more accurate at quantifying these theoretical parameters is because ACCext is the portion of the ACC transport due solely to buoyancy forcing, which is the *Lentz and Helfrich* (2002) theory is derived for.

Figure 3.17 shows these theoretical parameters as a time series calculated using the monthly mean data of the ACC using $\Delta\rho$ as the density difference between the bottom instrument at A2W and the upper instrument at A4 and Δv being the velocity between the lower instrument at A2W and the upper instrument at A4. On this longer timeframe, the observations do not match well with the theoretical parameters. In the first subplot of Figure 3.17, it is evident that the theory overestimates the depth of the ACC, as was found above.

In the second subplot of Figure 3.17, the theoretical estimates bound the observations (meridional mid-depth velocities at A4) relatively well, with c_α underestimating the observations 69% of the time and c_w overestimating the observations 54% of the time. We also show that c_p, the propagation speed of the nose, is always less than the observed velocity at A4. This is expected, as the velocity at A4 cannot be directly equated to propagation speed, as propagation speed of a buoyant current is not the same as the velocity recorded by one mooring at one point. However, since we have determined the ACC is surface-trapped, we know that the onshore quiescent region from the foot of the front will be relatively small. This means that less of the forward transport of the current will be transferred to filling in the onshore quiescent region (see

Figure 1.3), and therefore the propagation speeds (c_w and c_α) should be similar to the measured meridional velocities at mid-depth A4. Despite the fact we believe the ACC to be a surface-trapped, it is useful to compare the steep slope propagation speed (c_w) with the small bottom slope propagation speed (c_α) to determine how these parameters differ with our data.

Unfortunately, in the last subplot (current width), we have limited measurements that we can use to compare with observations. This was addressed in Section 3.1.2: Width.

The comparatively good agreement between theory and observation for the velocity likely reflects that strong control of geostrophy on current speed. But the poor agreement with depth suggests that critical features of the real-world strait are not reflected in the density-only model of *Lentz and Helfrich* (2002). We have seen above the importance of wind forcing on the velocities in the strait, and this forcing is absent from *Lentz and Helfrich* (2002). Thus, we consider next the theories of BCC which incorporate also wind forcing.

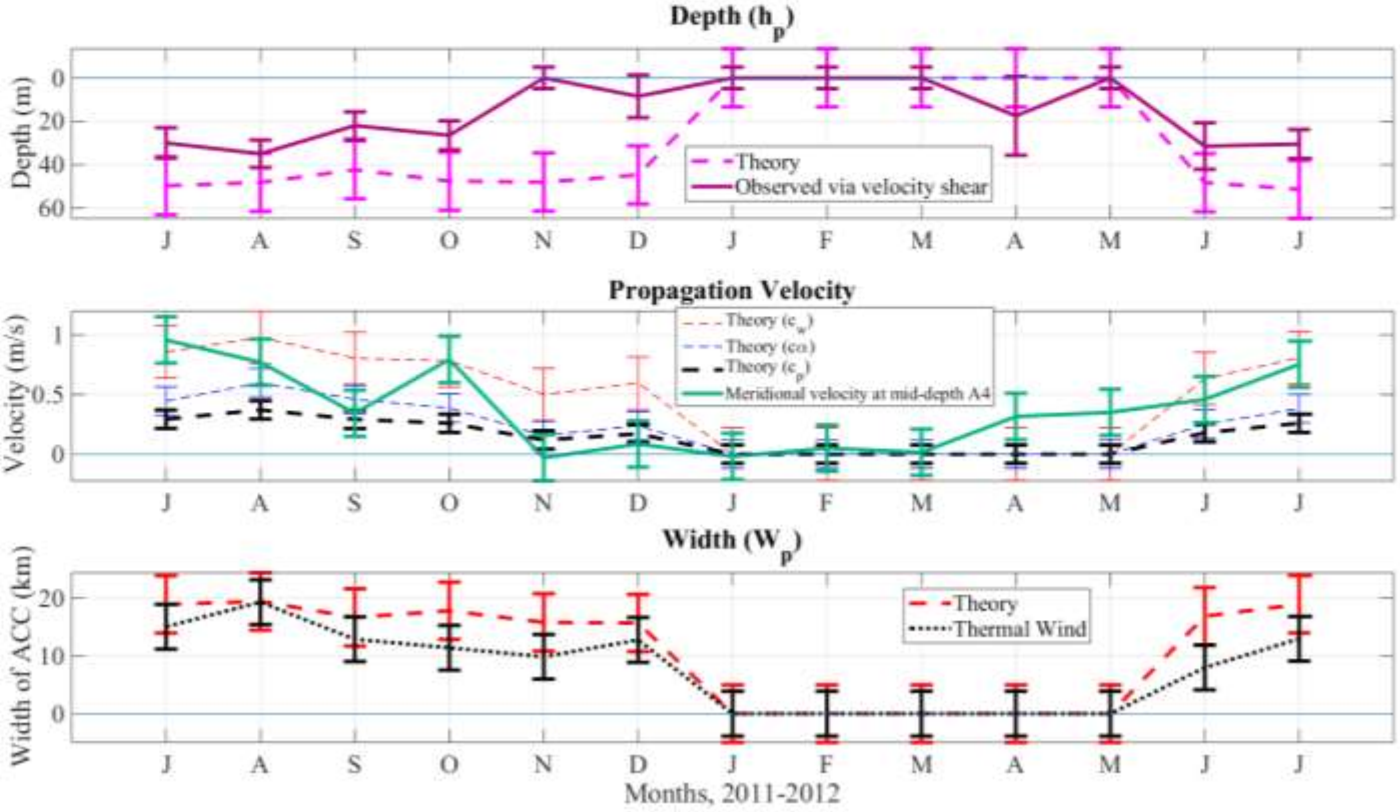

Figure 3.17: (a) Comparison of observed monthly averaged ACC depth to theoretical ACC depth using Equation 1.1 from Lentz and Helfrich (2002). (b) Comparison of observed monthly averaged velocity at 14 m from A4 with the theoretical propagation speed in the limit of a small bottom slope (c_α) using Equation 1.4 (blue dashed line), the theoretical propagation speed in the limit of a steep bottom slope (c_w) using Equation 1.3 (red dashed line), and the theoretical propagation speed if the bottom slope is neither steep nor small (c_p) using Equation 1.5 (black dashed line). (c) Theoretical width of the ACC using Equation 1.8 from Lentz and Helfrich (2002). We had too few measurements in order to determine observed widths of the ACC.

3.5: Quantifying the impact of wind on the ACC

Buoyancy or wind controlled?

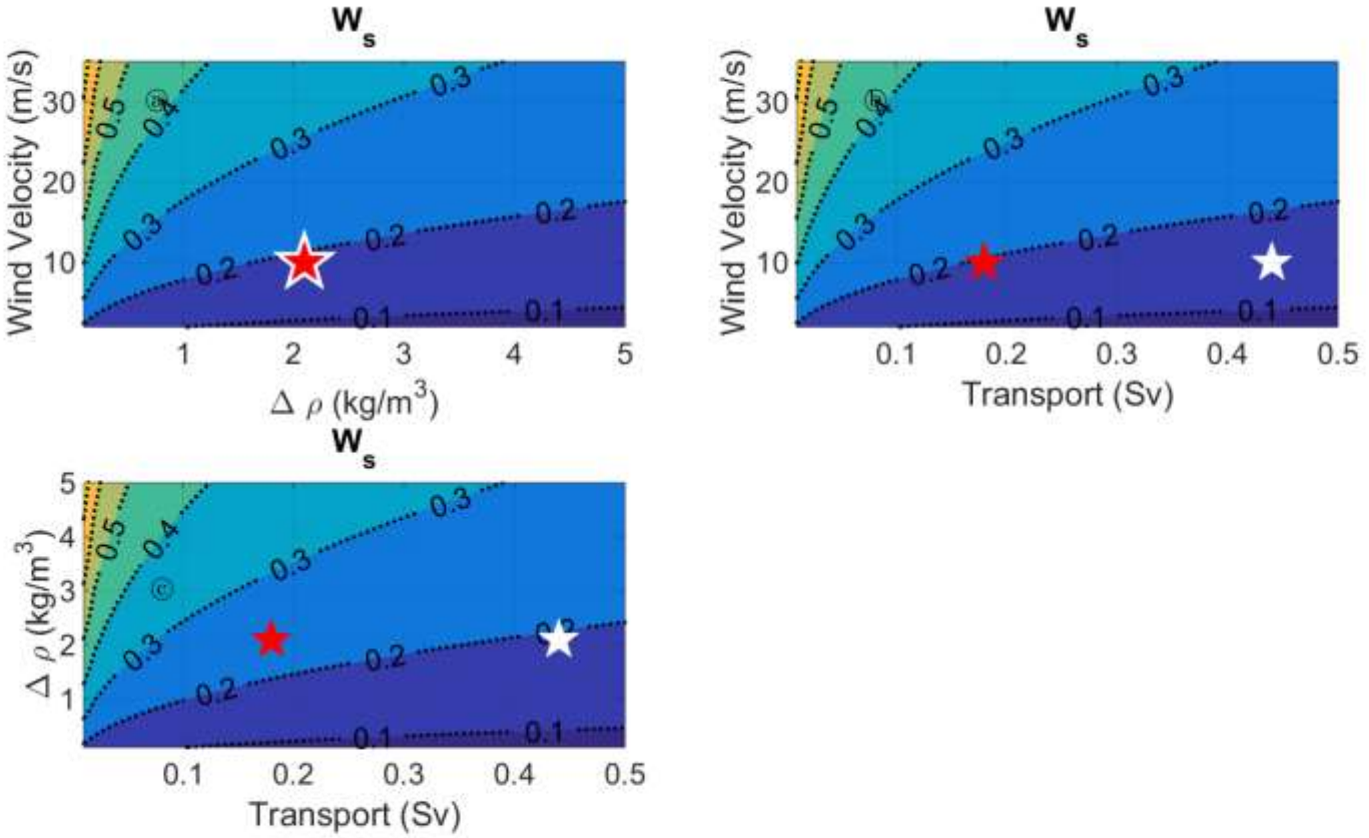

Figure 3.18: W_s (Equation 1.12) from Whitney and Garvine (2005). Each plot shows combinations of different variables as (a) wind velocity (m/s) on the y-axis and Δρ (kg/m3) on the x axis,(b) wind velocity (m/s) on the y-axis and transport (Sv) on the x-axis, and finally (c) Δρ (kg/m3) on the y-axis and transport (Sv) on the x-axis. The red stars represent average conditions in August 2011 (highest monthly averaged transport) for the transport that is due solely to the buoyancy forced velocity (ACCext), while the white stars represent the total transport of the ACC (ACC). When $W_s > 1$, the current is dominated by wind forcing, and when $W_s < 1$, the current is dominated by buoyancy forces. Note in all cases W_s is less than 1, suggesting the dominance of buoyancy forces. While these parameter intervals do not represent all ranges observed in the strait during the first summer to autumn of our record, they do represent the range of the monthly averages we see in the strait during that time.

We look next at the theories which include wind's impact on buoyant coastal currents (*Csanady*, 1977; *Lentz*, 2004; *Lentz and Helfrich*, 2002; *Lentz and Largier*, 2006; *Moffat and Lentz*, 2012; *Whitney and Garvine*, 2005). As discussed in Chapter 1, we assume that the background flow in the strait (i.e., the non-ACC velocity of the water column) can be represented by the water velocity at the bottom of A2W as this mooring is usually far enough west to be out of the influence of the ACC. The buoyancy driven velocity of the water column is reflected in the shallow velocity near the surface at A4, as this mooring is closest to the Alaskan coast and typically sits within the ACC. These two water velocities can be combined in Equation 1.12 (taken from *Whitney and Garvine* (2005)) in order to help us determine if wind or buoyant forces are more important driving factors in forcing the ACC. By considering the wind speeds, transports, and density anomalies present in the Bering Strait, we find that, in the Bering Strait in 2011, the current is always in a regime where $\mathrm{W}_s < 1$, meaning the ACC should, according to theory, be more driven by buoyant forces than by wind (Figure 3.18). This probably explains why the velocity agreed to some extent with the buoyancy theory of Lentz and Helfrich (2002) discussed in Section 3.4.

In order to validate the theoretical parameter in Figure 3.18, we used Equation 1.12, where we set the water velocity at mid-depth A4 equal to u_{dis} and the water velocity mid-depth at A2W equal to u_{wind}. From mid-July to the end of October 2011, when the ACC is strongest, we find the ACC is dominated by buoyant forces ($W_s < 1$) a vast percentage of the time (89%), with the buoyant forces being twice as big as the wind driven forces ($W_s < 2$) 34% of the time. This leads us to believe that buoyant forces are more important than wind forces when controlling the ACC, consistent with the wind strength index from *Whitney and Garvine* (2005) (Figure 3.18). This also is in agreement with previous studies, who found that the ACC near Barrow, Alaska was also buoyancy driven, with W_s values of ~0.5 (*Shroyer and Plueddemann*, 2012).

3.6: Separation of the ACC from the Alaskan coast due to southward wind

Previous work on Separation of ACC due to wind

There have been suggestions from observations that the ACC can become separated from the Alaskan coast (*Pisareva et al.*, 2015; *Woodgate et al.*, 2015) and, according to model results, remain separated for months (*Pisareva et al.*, 2015). *Pisareva et al.* (2015) analyzed hydrographic data from September 2009 that they suggest showed a bottom intensified ACC displaced to the far western side of the Bering Strait against the Russian coast, ~85 km from its normal position against the Alaskan coast. They concluded that an anomalously intense southward wind event during the time of their data collection in September 2009 was the causative factor for this separation of the ACC. They created a simple model to explain their observations. The model simulations showed that a strong southward wind could move the ACC to the Russian coast, and in their model, the ACC, once transposed, remained transposed for months. While this model provides some interesting results, it also has some unrealistic features. For example, they represent the mixed layer depth as <5 m in their model, whereas previous observations show much deeper mixed layers in the Chukchi Sea, averages of ~10-15 m over the summer months with individual measurements being twice as deep or more (*Peralta-Ferriz and Woodgate*, 2015; *Woodgate et al.*, 2015). These deep mixed layers dominate the density field of the strait, and thus a model which fails to recreate them is missing key features of the strait's physics. Their model also showed the current reverse directions only in a small portion of the core of the current during a simulated southward wind event (with wind speeds of 8.5 m/s), even though previous studies (as well as our work, see Figure 3.19) show that the flow through the strait both within and outside the ACC reverses direction with as little as 10 m/s of southward wind (*Woodgate et al*., 2005). During our analysis, we found that flow reversals typically occurred during winds as weak as 8 m/s (Figure 3.19). During southward Wind Event U2 (JD 247-252), discussed below, our mooring data showed the entire Bering Strait flow reversed to give southward flow of up to 1 m/s by the end of the third day (Julian day 249).

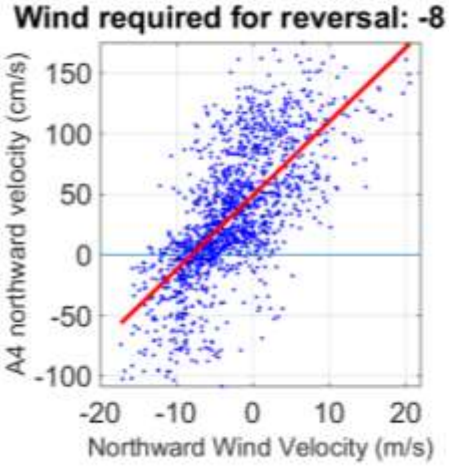

Figure 3.19: A4 water velocity at 14 m depth on the y axis with meridional wind velocity on the x axis. Best fit line in red shows a southward wind velocity of ~8 m/s is generally required to reverse the flow of water at A4 at 14 m depth.

Further investigation into ACC separation

In order to study the processes necessary to separate the ACC from the coast, we analyzed the three strongest southward wind events (Figure 3.20) in the beginning of our record during the summer through fall of 2011 that we thought may have resulted in a separation of the ACC from the Alaskan coast (Table 3.3). We say the ACC has separated from the coast if the ISCAT at A4 is measuring a denser value than moorings to the west. This provides a comparatively simple test of separation. It is also important to note that, because A4 is ~10.3 km from the coast, we may have missed a separation of the ACC if it was inshore of A4.

From observations of our density data, we found only the second and third southward wind events from Table 3.3 resulted in ACC separation (*Figure 3.21*). Table 3.3 collate details of each wind event, as well as important theoretical parameters and the values used to calculate them, which will be described in more detail shorty.

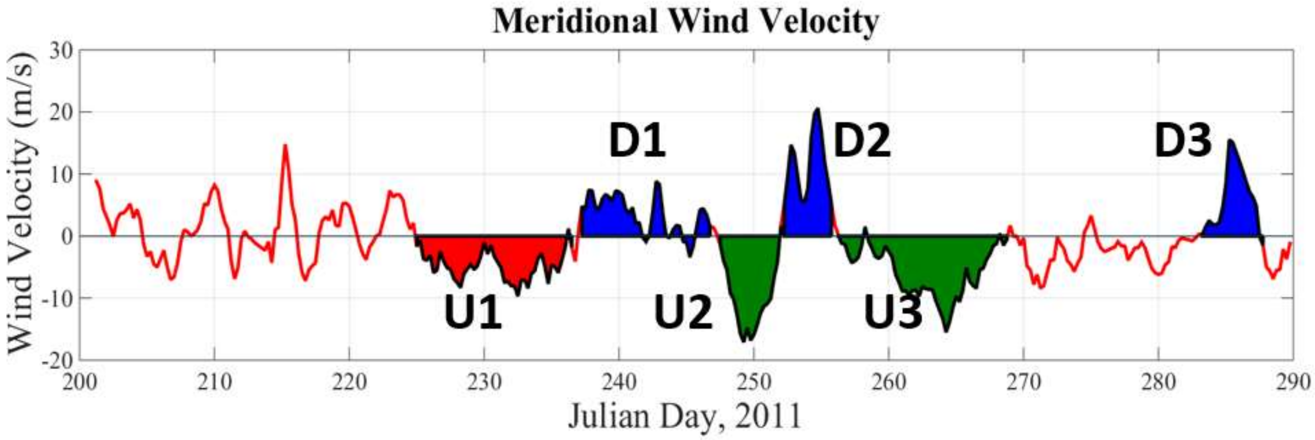

Figure 3.20: Southward wind events (colored red and green) during summer/autumn 2011. X axis is Julian day. Y axis is wind velocity (positive signifying northward wind). As discussed below, a red filled wind event means the ACC was not separated from the coast, while a green filled wind event means the ACC did separate from the coast. White text labels wind events as U1= southward Wind Event U1, U2= southward Wind Event U2, and U3=southward Wind Event U3.

Table 3.6:Southward Wind Events with Julian days in parenthesis. I and C are from Equation 1.10 and 1.11 in Chapter 1, respectively. Theory suggests I must be greater than C for separation to occur, and our observations concur with this theoretical prediction. t_{tilt} *is from Equation 1.13.* $\Delta\rho$ *refers to the density difference between the lower instrument at A2W and the upper instrument at A4. A negative wind velocity represents a southward wind. Asterisks show the authors responsible for each theoretical parameter.*

Southward Wind Events (Julian Days) -- Upwelling Winds--	Wind Event U1 (225-236)	Wind Event U2 (247-252)	Wind Event U3 (256-268)
Max wind velocity during event	-10 m/s	-17 m/s	-16 m/s
Average wind velocity during event	-5 m/s	-10 m/s	-6 m/s
Max $\Delta\rho$ during event	3.1 kg/m^3	3.3 kg/m^3	2.6 kg/m^3
Observed time for current to separate	Didn't Separate	60 hours	132 hours
Average velocity during separation	N/A	-8 m/s	-3 m/s
Max $\Delta\rho$ during separation	N/A	3 kg/m^3	2 kg/m^3
Theoretical parameters from Whitney and Garvine (2005)* and Csanady (1977)**			
Theoretical t_{tilt} *	21 hours	8 hours	42 hours
I (Integrated wind impulse) **	41 m^2/s	75 m^2/s	78 m^2/s
C (Minimum impulse required for full upwelling) **	45 m^2/s	44 m^2/s	36 m^2/s

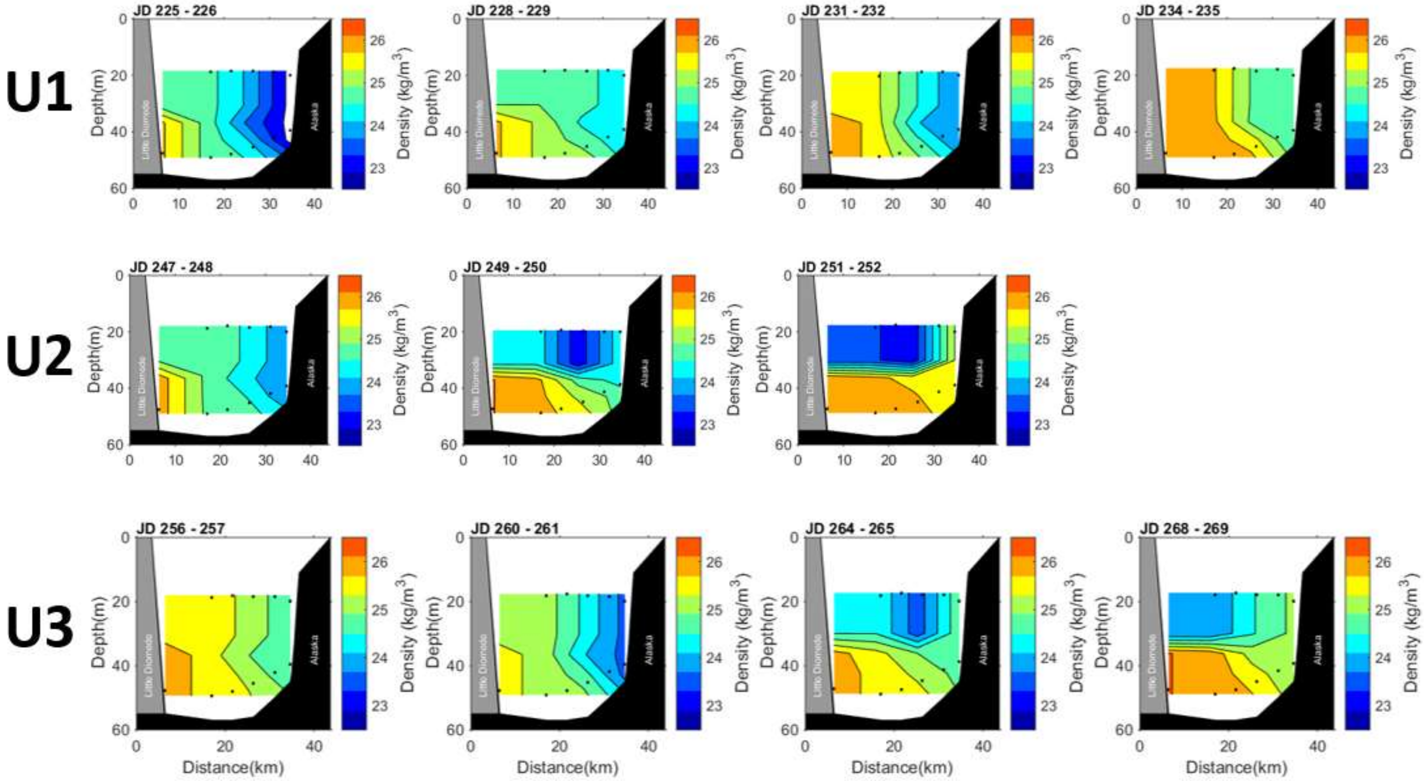

Figure 3.21: Evolution of specific days of daily averaged density field in the eastern Bering Strait during wind events as calculated from mooring temperature and salinity data. Each row represents a different wind event (see Table 3.3), and each panel shows a selected daily averaged density section within that event (Julian days are marked at the top of each panel). Notice the tilting of the isopycnals and the separation of the ACC from the coast in southward Wind Events U2 and U3.

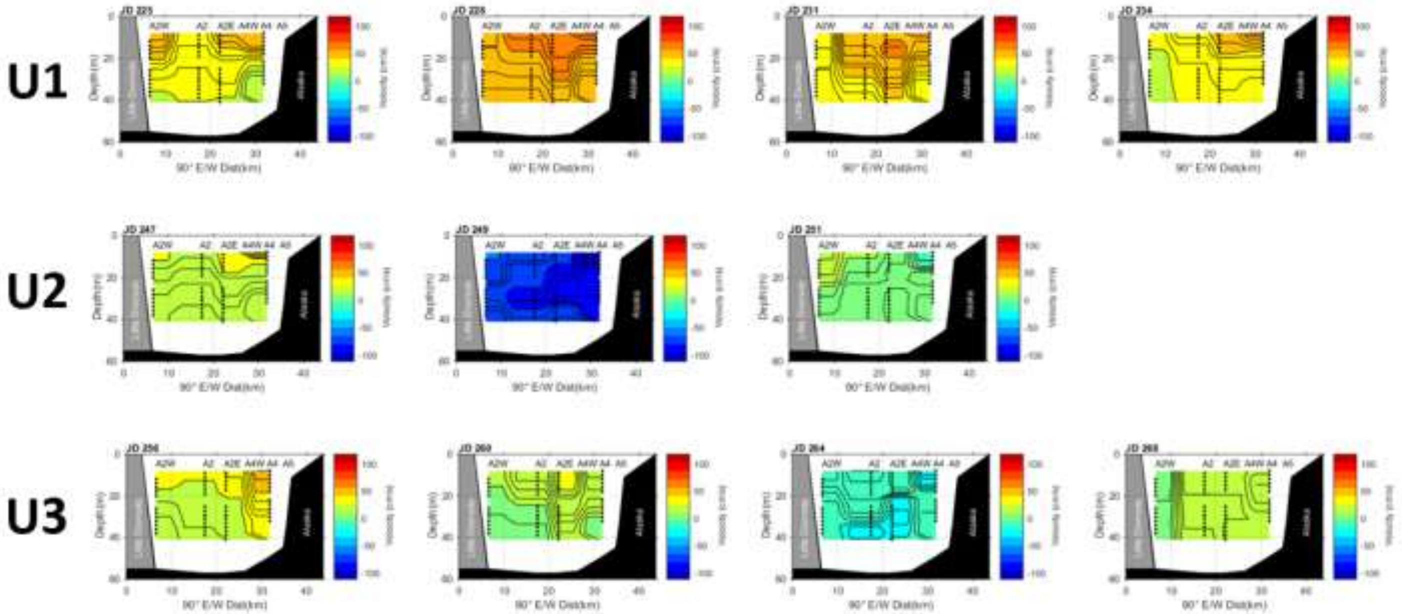

Figure 3.22: Evolution of specific days of daily averaged meridional velocity (positive is meridional) field in the eastern Bering Strait during southward wind events as obtained from ADCP data. Each row represents a different southward wind event (see Table 3.3), and each panel shows a selected daily averaged velocity profile within that event (Julian days are marked at the top of each panel). Notice how the core of the current separates from the coast at some stage during each event, despite the fact that the density profile did not separate in each event. This may reflect the theory of Lentz and Helfrich (2002) that inshore of the front the water flow may be less energetic (see Figure 1.3). Also notice the negative velocity scales towards the end of southward Wind Event U2 and U3, indicating the entire strait throughflow has reversed and become southward.

During southward Wind Event U2, we observe the ACC being separated from the Alaskan coast and dramatically slowed from northward flow of 50 cm/s (velocity data from ~10m at mooring A4) on Julian day 247 to a southward flow of -100 cm/s on Julian day 248 (velocity data from ~10m at mooring A4), while the flow in the eastern channel (velocity data from ~38m at mooring A2W) slows from ~15 cm/s to -70 cm/s southward on the same timeline. By Julian Day 249, almost the entire strait has reversed flow direction, with the ACC flowing southward at velocities of -30 cm/s and the ambient water flowing southward at velocities of ~0-5 cm/s.

Southward wind event U3 shows similar reversals, with the entire strait reversing flow after ~9 days (Figure 3.22).

In contrast, southward Wind Event U1 had weaker winds than Wind Event U2 and U3 and showed less dramatic impacts from the wind. During this wind event, the core velocity of the ACC was separated from the coast, however, the flow did not reverse and the density structure did not show a full separation from the coast (Figure 3.13 and 3.14). The ACC slowed from ~110 cm/s on JD 225 (velocity data from ~10m at mooring A4), to ~45 cm/s on JD 227 (velocity data from ~10m at mooring A2W), while the ambient waters slowed from ~40cm/s (velocity data from ~38m at mooring A2W), to ~20 cm/s (velocity data from ~38m at mooring A2W), on the same time line.

Following the theory of *Csanady* (1977) (Equations 1.8 and 1.9), we calculated for each of these wind events, the time integrated alongshelf wind stress (I) and the minimum impulse required for "full" upwelling (C). This theory suggests that only the second and third wind events should have separated the ACC from the coast, a result which is consistent with our observations.

Can we predict the combination of wind and duration that is necessary for separation? We can, by combining Equations 1.10 and 1.11 from Chapter 1 (I and C of *Csanady* (1977)). Thus, for a given period of time (Δt), we can derive the minimum wind speed required, viz:

$$U = \sqrt{\frac{\rho C}{\rho_{air} C_{10} \Delta t}} \tag{3.20}$$

where U is the minimum southward wind speed required for "full" upwelling (which in the Bering Strait would lead to the separation of the ACC from the coast), ρ is the average water density, C is the minimum impulse required for full upwelling from Equation 1.11, ρ_{air} is the density of air (1.2 kg/m^3), C_{10} is the drag coefficient (1.2 X 10^{-3}), and Δt is the amount of time the wind blows (*Csanady*, 1982). The tradeoff between wind speed and duration is shown graphically in Figure 3.15, where one sees that a wind duration of longer than 24 hours is required for any wind speed lower than 15 m/s to separate the ACC from the coast.

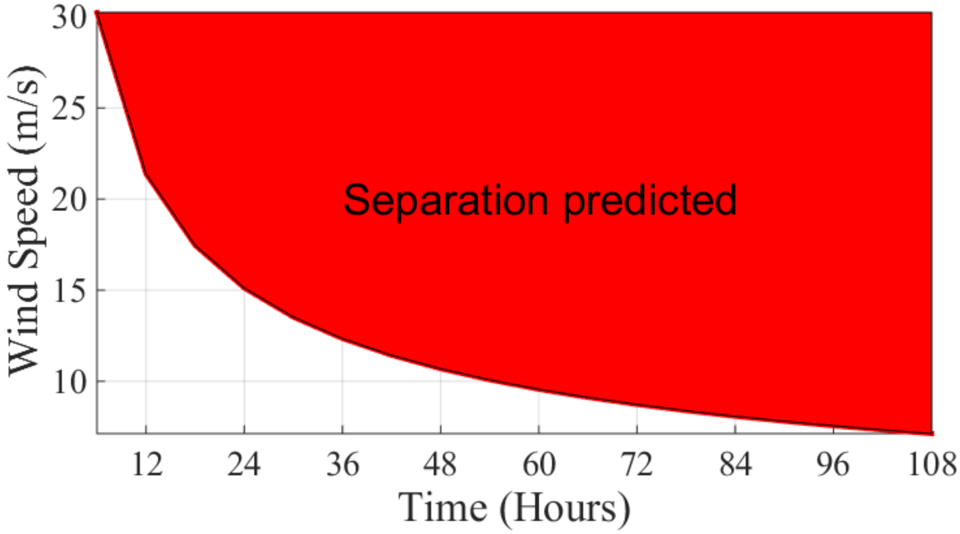

Figure 3.23: Using Equation (3.20) the area shaded in red shows the combinations of wind speed and wind duration that would result in separation of the ACC from the coast. Values for this plot are calculated using a background parameter of h_t (initial upper layer thickness, taken as 20m), h_b (initial bottom layer thickness, taken as 30m), and $\Delta\rho$ (density difference between the plume and the ambient water taken as 2.5 kg/m^3).

Timing of Isopycnal Tilting due to Wind

The ability to accurately predict how fast isopycnals will tilt due to wind forcing is important for quantifying a buoyant coastal current, as isopycnal tilting usually precedes separation from a coast. *Whitney and Garvine* (2005) develop a parameter that shows this called the wind adjustment time (t_{tilt}) as discussed in Chapter 1. The tilting refers to the time taken for the isopycnals to move such as to extend the current width by half or narrow it by half. In order to compare this theory with observations, we analyzed again the three strong southward wind events in Table 3.3. Due to our spatially limited measurements, it is difficult to accurately identify exact isopycnal tilt and current width, especially with the relatively small angle of tilt observed during southward winds (meridional wind isopycnal tilting is easier to identify, as discussed below in Section 3.7). Thus, instead, we will use the separation time observed in our data to compare with the theoretical t_{tilt} times, expecting the t_{tilt} times to be less than, but comparable to the separation time. As discussed above, our data show that only southward Wind Event U2 and U3 separated from the coast. We find that for the southward Wind Event U2, the observed separation time is 7 times larger than the theoretical t_{tilt} calculation (Table 3.3).

For the southward Wind Event U3, the observed separation time is more than 3 times larger. While these calculations do not verify the t_{tilt} parameter, they do show that the t_{tilt} time could be possible, as the tilting of isopycnals would occur before the current has separated from the coast.

These calculations also show t_{tilt} is more sensitive to the wind stress applied and less sensitive to the density anomaly, meaning a slight miscalculation in wind speed could drastically change our result, as shown by the ranges of values in the following contour plots of t_{tilt} for various $\Delta\rho$ and wind velocity combinations.

Another reason for the inaccuracy of t_{tilt} is because non-steady state conditions, such as our wind velocities, are difficult to quantify in observations when comparing to theories. The wind velocities typically start at zero and ramp up to a number higher than the average wind velocity used to make the t_{tilt} calculation. The density difference between the plume water and the ambient water also is not constant during our record leading to the same type of problem.

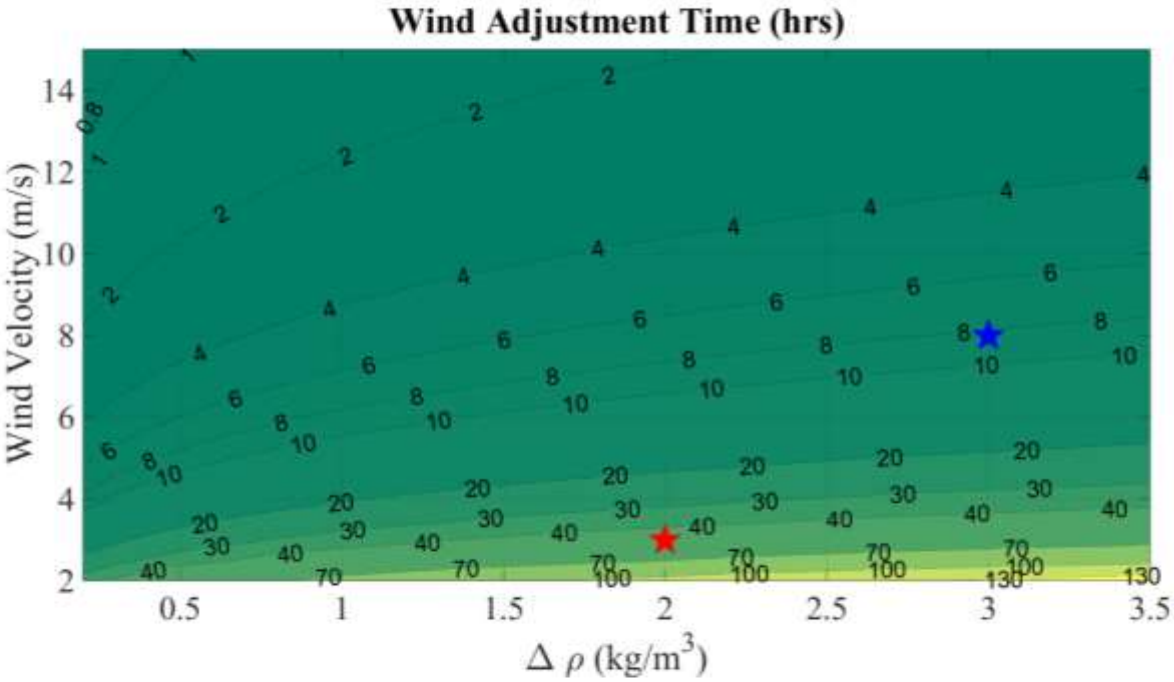

Figure 3.24: Wind adjustment time, t_{tilt} in hours from Whitney and Garvine (2005). This is the time it would take the wind to spread a current by half or narrow it by half. The blue star represents the wind and density anomaly present in the Bering Strait during Wind Event U2 which led to a separation of the ACC in ~60 hours. The red star is southward Wind Event U3, which led to a separation of the ACC in ~132 hours. Wind Event U1 did not result in a separation of the ACC from the coast.

3.7 Frameworks specific for downwelling winds

We have focused above on upwelling events. What of the downwelling events in the data? As mentioned in Chapter 1, *Moffat and Lentz* (2012) derive a theoretical framework for a downwelling wind's impact on a buoyant coastal current. Here, we will investigate an important parameter derived by *Moffat and Lentz* (2012) as discussed in Chapter 1. This is t_a, a timescale for the steepening process of the current's isopycnals (similar to t_{tilt} mentioned earlier in Section 3.6). t_a is a function of transport, density anomaly, and wind. While "steepening" is not precisely defined in their paper, we take it to mean a general tilting of isopycnals from an approximately 45^o angle to vertical. As noted previously, the tilting of isopycnals is difficult to observe given our sparse data coverage, however, the tilting of isopycnals during a northward wind is easier to identify, as vertical isopycnals show up clearly when the upper and lower instruments of the mooring record the same density. Due to this fact, the timing of our observations are approximations. Figure 3.17 shows three contour plots for different wind speeds of t_a using transport and density anomaly. You can see t_a is greatly dependent on the wind speed (given in the title of each plot) (Figure 3.17).

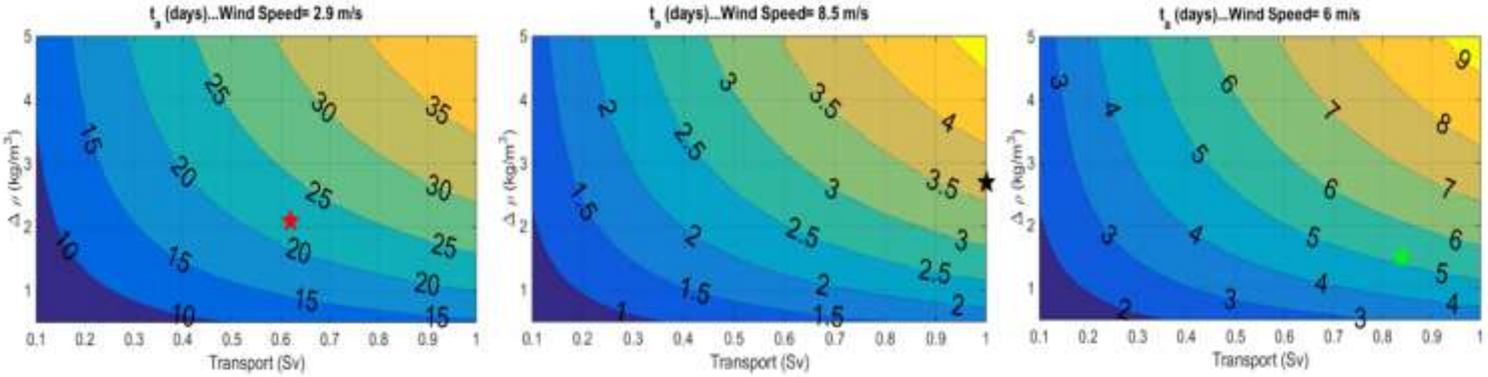

Figure 3.25: Parameter t_a given transport (Transport, x-axis) and density anomaly ($\Delta\rho$, y axis). The red star plot is for northward Wind Event D1 with average northward wind and $\Delta\rho$ across the strait, the black star is for northward Wind Event D2, and the green star is for northward Wind Event D3.

Similar to the investigation for the upwelling winds, for the downwelling winds we chose the three strongest downwelling (meridional) wind events to analyze in our record (Table 3.4). We compared the theoretical values of the t_a parameter to observations for these three downwelling (meridional) wind events (Table 3.7). Of the three wind events, only Wind Event D2 and Wind Event D3 clearly showed isopycnal tilting due to meridional winds. For Wind Event D2, the isopycnals tilted in ~2 days, during which time the average wind speed was 8.5 m/s and the maximum density anomaly was 2.7 kg/m^3. This produced a t_a (3.7 days) larger than compared with observations (≤ 2 days) and a theoretical t_{tilt} value much smaller than observations (7 hours). We found that for Wind Event D3, the theoretical t_a is 5.2 days compared to the observed tilting time of ≤ 3 days and a t_{tilt} value much smaller than observations as well (10 hours) (see Table 3.7). t_a, unlike t_{tilt} which underestimates the timing of isopycnal tilting, seems to overestimate the observed results by a factor of 2 in each case, so while these t_a numbers are larger than the times we estimate from the data, they are comparable to the timescales observed.

One reason that this theoretical framework may not be matching observations is because the theory assumes constant vertical and lateral density gradients, which is a poor approximation for the Bering Strait. This limitation is clearly acknowledged by the authors, who note that "buoyant plumes can have a sharp frontal structure separating the ambient water from the fresh coastal water and is not constantly stratified as assumed…" (*Moffat and Lentz*, 2012). From the sparse CTD sections we have of the ACC (Figure 1.2) and our mooring data, it seems that this assumption does not hold for our current.

Finally, we also use the meridional winds to validate t_{tilt}, as this parameter was not specific to upwelling or downwelling winds (see Table 3.7 for results). As with the southward winds, t_{tilt} dramatically underestimates the time we observe the isopycnals to tilt (Table 3.6). The reasons for this underestimation are most likely the same reasons as discussed with the southward wind condition, i.e., our wind, transport, and density difference between the plume and ambient waters are a function of time, and are not constant. We conclude that t_a seems to be a more accurate indication of isopycnal tilting times when compared to t_{tilt}.

Table 3.7: Major meridional wind events during summer/fall of 2011. t_{tilt} *is from Equation 1.13.* t_a *from Moffat and Lentz (2012) . The observed time to separate was calculated by density separation from coast. Asterisks show the authors responsible for each theoretical parameter.*

North Wind Events (Julian Days) --Downwelling Winds--	Wind Event D1 (236-247)	Wind Event D2 (252-256)	Wind Event D3 (283-287)
Max wind velocity during event	9 m/s	21 m/s	16 m/s
Average wind velocity during event	2.9 m/s	11 m/s	7 m/s
Max Δρ during event	3.1 kg/m^3	3 kg/m^3	1.7 kg/m^3
Observed isopycnal tilt time	None	≤ 2 days	≤ 3 days
Average transport during tilt	0.6 Sv	1 Sv	.8 Sv
Average Δρ during tilting of isopycnals	2.1 kg/m^3	2.7 kg/m^3	1.5 kg/m^3
Average winds during tilt	2.9 m/s	8.5 m/s	6 m/s
Theoretical parameters from Whitney and Garvine (2005)* and Moffat and Lentz (2012) **			
Theoretical t_a **	20.1 days	3.7 days	5.2 days
Theoretical t_{tilt} *	53 hours	7 hours	10 hours

3.8: Ekman dynamics across the entire eastern channel of the strait

We have focused above on the response of the ACC to wind, but this response will not be in isolation. One might expect a response of the entire strait to upwelling and downwelling winds. During a strong southward (upwelling) wind, one would expect that surface Ekman transport moves water away from the Alaskan coast, creating upwelling and a counterclockwise circulation (looking northward) throughout the entire water column. The opposite circulation would be expected during the set up from a downwelling wind, and this is shown schematically in Figure 3.26.

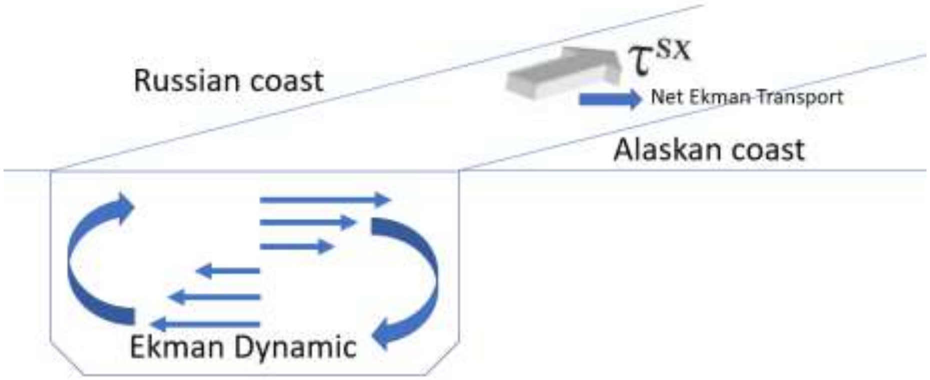

Figure 3.26: Ekman dynamics in the Bering Strait during a downwelling situation due to a northward wind.

This cross-strait circulation is clearly seen in the rotated cross-strait velocity from the moorings, for example, under the southward Wind Event U2, shown here as Figure 3.*27*.

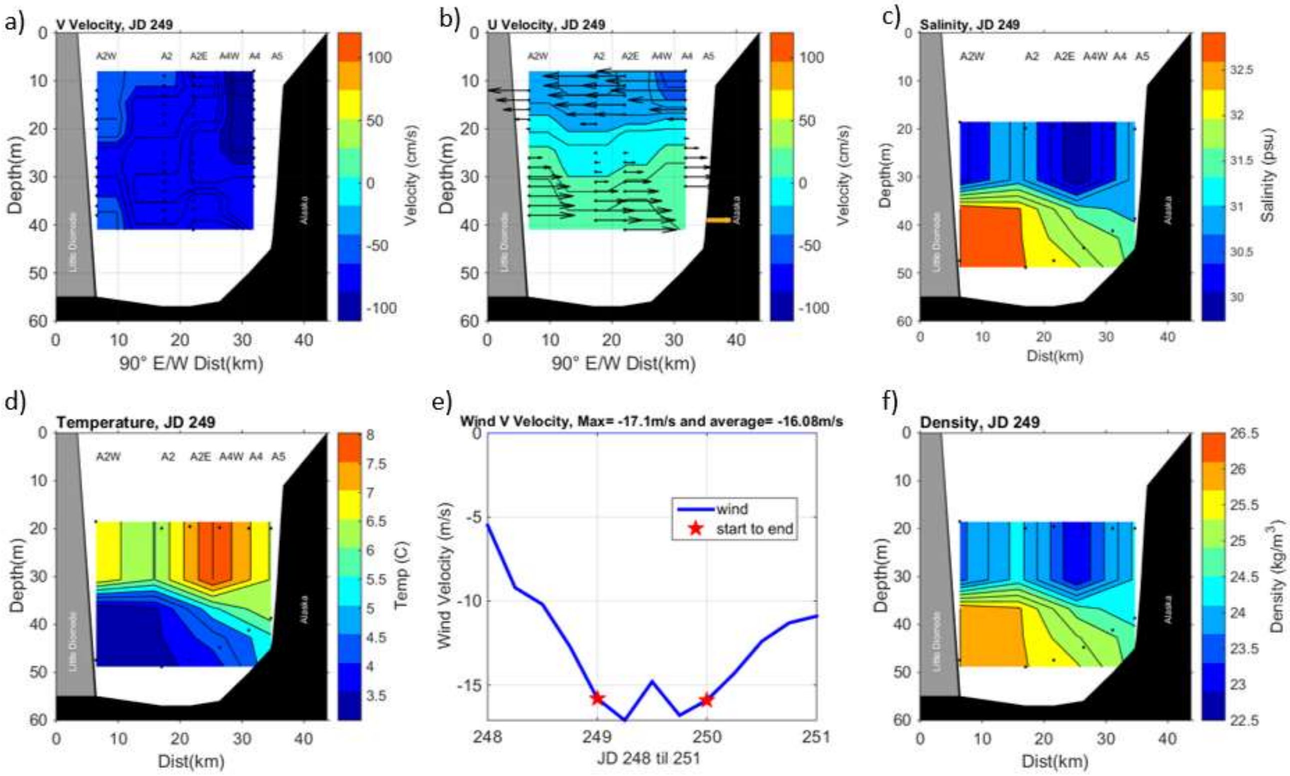

Figure 3.27: Showing observations during the middle of Wind Event U2. From top to bottom, left to right, a) Cross section of daily averaged rotated meridional velocity (vvel) in the eastern Bering Strait, b) Cross section of daily averaged rotated eastward velocity (uvel) in the eastern Bering Strait, c) Cross section of daily averaged salinity in the eastern Bering Strait, d) Cross section of daily averaged temperature in the eastern Bering Strait, e) time series of meridional wind velocity, with the red stars showing the start and end of the period used for the statistics of maximum wind velocity and average wind velocity, marked at the top of the panel, f) Cross section of daily averaged density in the eastern Bering Strait.

Surface Mixed Layer and Ekman Layer

Another parameter we are able to estimate using theory is the depth of the Ekman layer due to downwelling wind forcing. As per *Moffat and Lentz* (2012), we assume the mixed layer depth and the Ekman layer depth are approximately the same (however the Ekman layer depth can be deeper than the mixed layer depth). In order to compare an observation to the theoretical Ekman layer depth, we identify the mixed layer depth from our ADCP velocity data as the depth at which the rotated eastward velocity (the cross-strait velocity) changes sign from positive to negative in the two-layer system. We use velocity instead of density differences to mark the

Ekman layer, as we only have two density measurements in the vertical (lower and upper instruments), not enough to constrain the mixed layer depth in a useful way. During Wind Event D2, using an eastward velocity section (not shown), our analysis shows that the depth of the mixed layer is ~16m (taken from A2E). Using Equation 31 from *Moffat and Lentz* (2012) for the Ekman depth during a downwelling wind, we calculate the Ekman depth as a function of wind, density anomaly, and transport to be ~9m to 17m, consistent with observations (conditions during Wind Event D2 are marked as a red star in *Figure 3.28*).

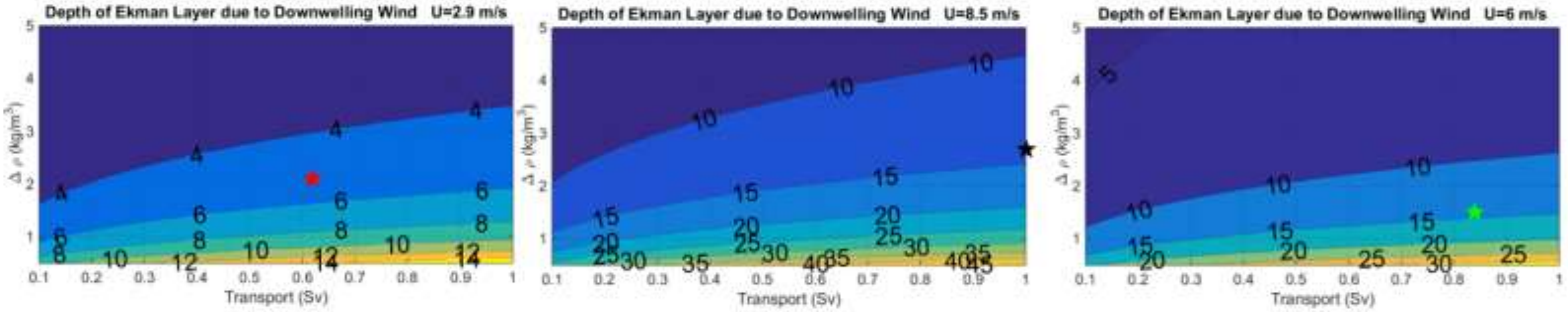

Figure 3.28: Ekman Depth given transport and density anomaly. This is using a constant wind speed of 2.9 m/s (left), 8.5 m/s (center) and 6 m/s (right), using the theory of Moffat and Lentz (2012). The red star marks the conditions during northward Wind Event D1, black is Wind Event D2, and green is Wind Event D3.

3.9: Source of ACC waters?

The source of water that forms the ACC is, to our knowledge, relatively unknown, and this section hopes to shed light on that question. *Aagaard et al.* (2006) show that the waters of the Bering Strait, and therefore the freshwater transport of the ACC, must be, in part, due to river runoff into the Bering Sea, as the waters of the Bering Sea are more saline than the ACC (*Aagaard et al.*, 2006). *Aagaard et al.* (2006) also cite river runoff to the Bering shelf is ~320 km^3/yr, made up of ~200 km^3/yr from the Yukon River, ~30 km^3/yr from the Anadyr River, ~75 km^3/yr from the Kuskokwim, Nushagak, and Kvichak Rivers, and ~10-20 km^3/yr from other ungauged streams. All the rivers (apart from the Anadyr) are in the USA. We do not take into account the freshwater discharge due to the Anadyr River, as it is on the Russian side of the strait, and the method for the water to reach the ACC on the eastern side of the strait is not physically clear. We also do not consider freshwater due to precipitation, as the yearly amount in the region is low (~80 km^3/yr) which is less than the Yukon's input and is spread over a much wider area of the Bering Sea.

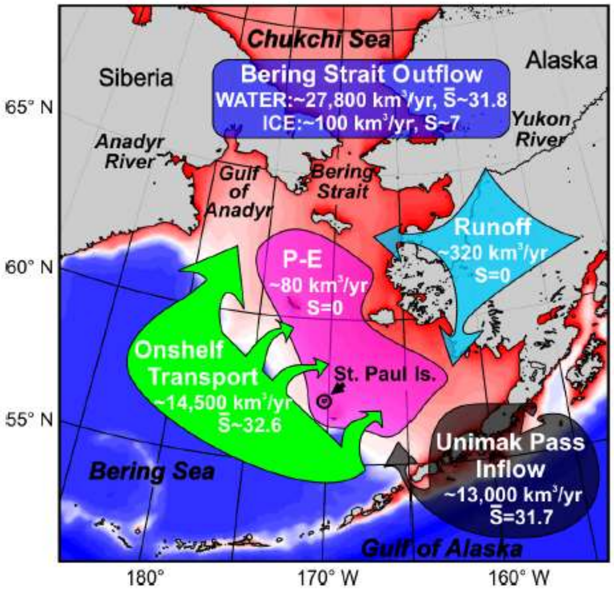

Figure 3.29: Reproduced from Aagaard et al. (2006). The Bering Strait shelf water and salt budgets.

The largest river, by far, that contributes to the runoff from the Seward Peninsula in Figure 3.29, is the Yukon River. Daily discharge data for the Yukon is only available for part of our study period (July to October 2011), thus we use also the USGS 39-year median discharge data for the Yukon River from Pilot Station, Alaska (https://nwis.waterdata.usgs.gov/nwis), to correlate the Yukon River discharge with two different measures of ACC freshwater transport. The first transport set of values we used are the ACC values calculated as per Chapter 2.6. To compare to prior work, we use also a second set of values, viz the ACC transport as estimated by Woodgate (2018), i.e., multiplying the mid-depth ADCP bin from A4 multiplied by the cross-sectional area of 0.4 km^2, which is the approximate cross-sectional area of the ACC (as per *Woodgate* (2018)). Then, for each set of total transport values, we calculate the equivalent freshwater transport for the ACC:

$$T_{FW} = T_{vol}(1 - \frac{S}{S_{ref}}) \tag{3.21}$$

Where S is the salinity of the upper level instrument at A4 (as we believe that to be a proxy for the ACC's salinity), and T_{vol} is the volume transport of the ACC, and T_{FW} is the freshwater transport relative to a reference salinity S_{ref}. We take as the background salinity ($S_{ref} = 32.5\ psu$) an estimate of the mean salinity of the non-ACC Bering Strait throughflow, i.e., the average of the monthly averaged salinity from the beginning of our record (July 16th 2011) till the end of December 2011.

We consider first the time variability of the freshwater signals. We found that the highest correlation (r =0.75, correlation significant above the 95% level ($p \leq 0.05$) occurred with a 12 to 15-day lag between the Yukon River discharge (39-year median daily discharge) and the ACC freshwater transport estimates (Figure 3.30) (with the Yukon leading the ACC freshwater). This corresponds to a water velocity of approximately 40 cm/s over the distance of ~450 km (a rough estimate of the flow pathway from the mouth of the Yukon to A4 from Google Earth). *Clement et al.* (2005)'s 23-year modeled mean circulation in the upper 50 m suggests water velocities between the Yukon River mouth and the Bering Strait are between ~25 cm/s to 50cm/s, consistent with the most correlated lag we found.

In terms of freshwater volume, we find that, at this optimal lag, the ACC freshwater content (peaking around 0.03 Sv of freshwater relative to 32.9 psu), was greater than the Yukon freshwater (peaking at 0.01 Sv of freshwater). Thus, it seems the Yukon river (either the 39-year median daily transport or the 2011 data) cannot account for the total amount of freshwater seen in the ACC. In fact, in order to account for the freshwater in the ACC throughflow, we need ~10,000 m^3/s more freshwater volume transport at peak. Can we get this from other Alaskan rivers in the area? Probably not, as other rivers account for only ~90 km^3/year (3800 m^3/s) according to *Aagaard et al.* (2006), less than half of the missing freshwater (Figure 3.22).

Another possible freshwater source for the ACC is water from Unimak Pass in the Aleutian Islands, this flow being a side branch of the *Alaska* Coastal Current (not the *Alaskan* Coastal Current). We find that using Equation 3.5 with a yearly average of salinity in Unimak Pass as 31.7 psu (*Aagaard et al.*, 2006), and a reference salinity of 32.2 psu (the average salinity at the lower instrument at A2W from the beginning of our record till the end of December 2011), Unimak Pass supplies approximately 7,700 m^3/s of freshwater, still not enough on its own to account for the freshwater of the ACC.

However, if we add the freshwater transport from the Yukon discharge (39-year median daily discharge), the other Alaskan rivers (but not the Anadyr) mentioned in *Aagaard et al.* (2006), and the Unimak Pass, we get much closer to matching the freshwater needed to equal the freshwater transport of the ACC.

Note these calculations are sensitive to the reference salinity used, both for the ACC and the Unimak pass estimate. If, for example, we take a fixed salinity of 32.2psu to estimate the ACC freshwater, the ACC freshwater estimates decrease by ~20%. Despite this large change given the reference salinity, the general message is still the same, viz the Yukon, other rivers, and the Unimak Pass inflow likely all contribute to the freshwater of the ACC in the Bering Strait.

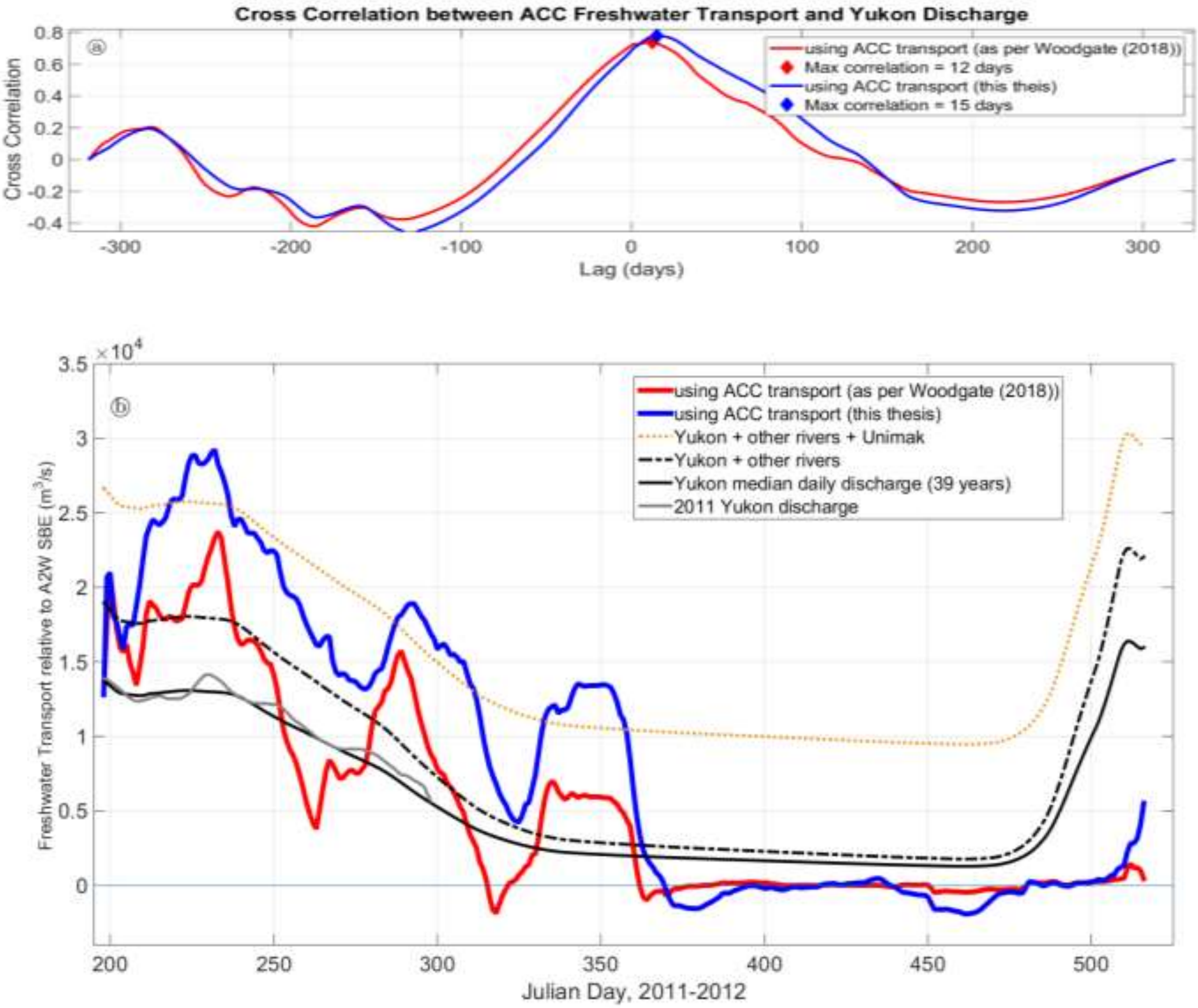

Figure 3.30: (a) Cross correlation between ACC freshwater transport and Yukon River discharge. The diamonds mark the highest correlations. (b) Combination of different freshwater sources that could make up the ACC, as well as ACC freshwater sources. The black line is the median daily discharge (39 years) of the Yukon River, while the two different 30-hour smoothed ACC freshwater discharge calculations are the red and blue lines. The gray line is the daily averaged 2011 Yukon River discharge. The dashed black line is the Yukon and the other rivers mentioned in Aagaard et al. (2006) added. The gold -- line is the Yukon River median daily discharge (39 years), Unimak Pass, and other rivers mentioned in Aagaard et al. (2006) added together. These freshwater calculations are relative to the average of the monthly mean salinity from the beginning of our record until the end of December 2011 at the lower instrument at A2W (32.2 psu). Note the other Alaskan rivers have been scaled to match the same annual profile as the Yukon River.*

3.10: Estimating ACC transport, freshwater transport, and heat only from A2 and A4

The 2011-2012 mooring coverage in the strait was remarkable, as typically only A2 and A4 are deployed in the strait. This extra coverage allowed us to pose the question: what is the difference in estimating the ACC transport using solely A2 and A4 versus using four ADCPs (A2W, A2, A2E, and A4)? Prior work (Woodgate (2018)), as discussed in the last section, estimated the ACC transport very simply i.e., assuming a fixed cross-sectional area of 0.4 km^2 for the ACC and multiplying that by the mid-depth meridional velocity at A4. But this assumes a fixed cross-sectional area for the ACC. A better estimate is likely obtained using a simplification of the box scheme we used in Section 2.6, i.e., using two horizontal divisions splitting the eastern Bering Strait (one for A2, one for A4), rather than four in the case when we use all moorings with ADCPs for transport calculations. In this case, we use the vertical box dimensions as before, related to the 2m bins of the ADCP data.

Results for all these calculations are shown in Figure 3.31- our best estimate (from all 4 moorings, in gray), the "Full" transport (transport calculated using all four ADCPs during our study year) minus our simple estimate using the box method with just A2 and A4 in red, and the Full transport minus the Woodgate 2018 method in blue. We found that when using solely A2 and A4, the transport values for the first 90 days of our data (July-October 2011) were 12% lower than the transport values calculated using all four ADCPs (Figure 3.31). When comparing the last 56 days of the record (May-July 2012), we find that A2 and A4 transport calculations underestimate our Full transport by ~38%. We also found that the Woodgate (2018) method captures even less ACC transport, by underestimating the Full transport by 38% and 30%, in the first 90 days and 56 days, respectively. The error in the transport calculations has previously been cited as ~25% (*Cooper et al.*, 2016; *Woodgate*, 2018), so differences of 12-38% may not be within these errors.

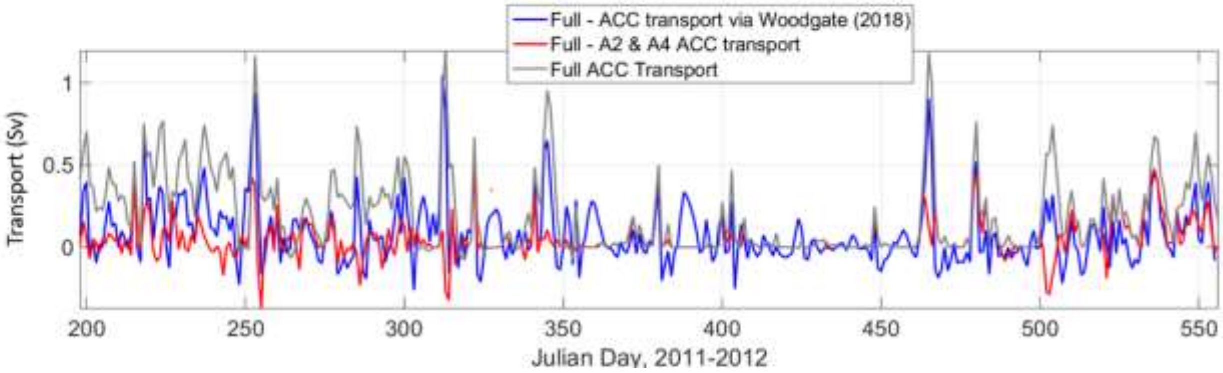

Figure 3.31: Difference in transport calculated using our 2011-2012 full mooring array (labeled "Full" here) minus the transport calculated via Woodgate (2018) in blue. Full transport minus the transport calculated with just A2 and A4 in red. For the first 90 days of the time series, the transport calculated at A2 and A4 (red line) underestimates the Full transport by 12%, and the transport calculated using Woodgate *(2018) underestimates the Full transport by ~38%.*

These results show us a few things, namely that parts of the ACC can sometimes reach the A2W ADCP, which increases overall transport when compared to using the ADCPs solely at A2 and A4. We also conclude that using a fixed cross-sectional area of the ACC to calculate transport misses changes in the ACC's width which we are able to measure more effectively using our box method.

4.1: Summary

We use data from seven moorings in the eastern Bering Strait to study properties of the Alaskan Coastal Current (ACC) from July 2011 to July 2012.

The ACC is a seasonal, mostly surface-trapped buoyant coastal current on the eastern side of the strait. During our study year (July 2011 to July 2012), the ACC was strongly present from July-August 2011, almost completely absent by November, then increasing again slowly at the beginning of May 2012. The highest monthly averaged transport of the ACC was during August 2011, at 0.44 ± 0.06 Sv. In that month, the monthly mean salinity and temperature across the eastern strait varied widely, up to ~2 psu and ~4º C, with extreme values in the ACC of 30.5 psu and 7.5º C. The depth of the ACC in this month was approximately 35 m as estimated from velocity shear. The width of the ACC was difficult to quantify due to our limited spatial variability across the strait, however from the CTD section taken during on July 16th 2011, we estimated the ACC width to be ~13 km. During the winter months, the strait becomes relatively homogenous in salinity and temperature and the entire strait experiences an increase in salinity most likely due to ice formation.

Consistent with past studies, year-round wind and water velocities are highly correlated (r= 0.7). We find the wind can significantly impact the current's parameters through Ekman transport, with strong and persistent (e.g., > 8 m/s over a period of ~60 hours) southward winds able to reverse the flow of the strait to yield southward ACC speeds of up to 1 m/s. A singular value decomposition of the northward rotated water velocities (i.e., parallel and perpendicular to the principal component of velocity) confirmed that the dominant spatial variability of the eastern channel of the Bering Strait is the strong signal of the ACC. The first mode of the empirical orthogonal function was highly correlated (r= 0.71) to the meridional wind, accounting for ~50% of the data's variance.

Many theoretical parameters from the literature for buoyant coastal currents, and buoyant coastal currents under the influence of wind were tested using our mooring observations. We find theoretical parameters for depth (h_p) which neglect wind forcing (*Lentz and Helfrich*, 2002) overestimate the observational estimates. However, we find the theoretical estimate for the propagation speed of the nose of the current (c_p) is less than the observed velocity of the ACC, as we expect, since a point measurement is not a good indicator of the nose speed. Using observed values, theory suggests the ACC is mainly buoyancy driven (not wind driven), and using theories which combine wind and buoyancy, we can also calculate two different theoretical times for tilting of isopycnals due to wind- t_{tilt} (*Whitney and Garvine*, 2005), which largely underestimated (by a factor of seven) observed times, and t_a (*Moffat and Lentz*, 2012), which overestimated observed parameters, but only by a factor of ~two. For t_a, the inconsistencies with the observations may be due to the observed density structure of the current not matching the assumed linear density structure in the theory (*Moffat and Lentz*, 2012). We also studied a parameterization from *Csanady* (1977) of the wind's ability to upwell a pycnocline. We found this is an accurate way to estimate if a southward wind event will separate the ACC from the coast.

Furthermore, we find the median daily discharge (39-years) of the Yukon River is highly correlated (r =0.75) with the ACC's freshwater transport if offset by 12-15 days. In order to match the volume of the observed freshwater discharge of the ACC, we found we require the freshwater discharge of all the rivers from the Seward peninsula (including the Yukon) as well as the freshwater transport through Unimak Pass in the Aleutian Chain, south of the Bering Sea.

Lastly, we found that our model improved upon the previous basic method for estimating ACC transport from *Woodgate* (2018) by ~38%.

4.2: Future Work

One of the most important parameters to define which we were unable to quantify in a satisfactory manner from our horizontally limited mooring measurements was the width of the ACC. We found that using velocity shear between the upper and lower velocity bins at a mooring site provided a rough estimate as to which mooring the ACC was between. However, as our moorings are spaced many kilometers apart (some ~10 km), there are large uncertainties in determining the current width using this method. Being able to accurately quantify the width of the ACC is important for all calculations in the strait, including freshwater and heat fluxes. Future studies may try to address this using high resolution sea surface temperature (SST) data (e.g., infrared satellite data). However, there are complications with this- clouds in the strait reduce the days SST data are available. Also, we observe the warm waters of the current detach from the coast into the strait under certain wind conditions, which may complicate identifying the front of the current.

A second limitation with the work presented in this thesis is to what extent our results represent typical parameters of the ACC, as we know that interannual variability of flow in the strait is high. From analysis of mooring data in the strait from 1990-2015, we are aware that 2011 was a high flow year and 2012 was a low flow year (*Woodgate*, 2018). The fact that our data exists during two anomalous years of high and low transport may mean that our results contain a large spectrum of the normal habits of the ACC. In addition, the extent to which we have been able to validate the predictions of theory may help extend our results to conditions in other years. Ultimately, however, the only way to confirm this is through future high-resolution studies of the ACC.

As described in this thesis, wind can drastically impact the parameters of the ACC. Most of the theoretical calculations we conducted are dependent on their relationship with the wind. In this thesis, we rely entirely on wind reanalysis data from NCEP, however, it should be remembered that these are themselves model results which may poorly represent reality. A preliminary study of this (Woodgate, 2018) show significant discrepancies between reanalysis products and the rare local wind data from Wales Airport, on the east coast of the Bering Strait. It would thus be productive to perform a more thorough analysis of the reanalysis data with any available data sources, e.g., wind data from local ships or research vessels that regularly transit the area. This could be a low-cost method, as most ships are already equipped with anemometers.

A large part of this thesis was testing theoretical parameters, many of which did not match observations very closely. For example, we validated two different parameters, t_a and t_{tilt}, both variables that quantify the amount of time required for isopycnals to tilt due to a given wind forcing and initial parameters of the current. We found that t_{tilt} underestimated the observed value by a factor of seven, while t_a overestimated the observations, but only by a factor of two. We also found the theoretical parameter which estimated the current's depth was inaccurate compared to observations. While there are many reasons the theoretical parameters may not have matched observations (i.e., inaccurate data, assumed density structure was not realistic, theory may be inaccurate), we are unsure of the final reason for the inconsistencies.

While we were able to compare the transport estimates of the ACC using all moorings with the transport estimates of the ACC using solely A2 and A4, an obvious extension of the current work would be to complete this same type of calculation for the freshwater and heat fluxes. This is an important question that should be answered in future studies.

The upper layer (<18 m) of the Bering Strait is not sampled in our thesis apart from two CTD sections in July 2011. From these CTD sections, it looks as though the upper instrument data are still greatly underestimating the surface temperature, salinity, and density, sometimes by as much as 3º C and 2 psu. This is because our upper instrument sits at ~18 m depth for most moorings, meaning we are not capturing any variability in the upper 18 m of the water column. While we do have ADCP data that reaches closer to the surface (~8 m), the water property data not captured in the upper 18 m of the strait could drastically change some of our theoretical calculations. A possible solution to this could be the use of satellites to collect data for sea surface temperature and possibly salinity. With these data points, it might be possible to interpolate between the surface and the upper instrument at each mooring.

With the use of the highest-resolution mooring array since records began, we provide a more detailed understanding of the ACC by employing new techniques that seek to quantify the ACC's parameters. We improve estimates of ACC transport by ~34% during peak summer months and also provide detailed snapshots into the system dynamics, including ACC upwelling events, ACC reversals, as well as classic Ekman circulation dynamics. Many of the physical dynamics of the current and region we observe in this thesis were first observed by the local population, and were noted for their importance for upwelling marine organisms for subsistence fishing practices, but also the danger associated with the rapidly changing environment (*Raymond-Yakoubian et al.*, 2014). We also validate many theories, including an estimation of the southward wind forcing and duration required to separate the ACC from the coast. Another important analysis is on the freshwater sources of the ACC, identified as not just the waters from rivers in Alaska, but also a sizeable contribution from the Unimak Pass.

This thesis has improved our knowledge of the ACC forcing factors, which are vital to better our understanding of the Arctic heat and freshwater budgets, and possibly, global climate.

Acknowledgments:

The Bering Strait mooring program is supported by NSF Office of Polar Programs' Arctic Observing Network grants PLR 1304052 and PLR 1758565.

References

Aagaard, K., and E. C. Carmack (1989), The role of sea ice and other fresh water in the Arctic circulation, *Journal of Geophysical Research*, *94*(C10), doi:10.1029/JC094iC10p14485.

Aagaard, K., T. J. Weingartner, S. L. Danielson, R. A. Woodgate, G. C. Johnson, and T. E. Whitledge (2006), Some controls on flow and salinity in Bering Strait, *Geophysical Research Letters*, *33*(19), doi:10.1029/2006gl026612.

Ahlnäs, K., and G. R. Garrison (1984), Satellite and Oceanographic Observations of the Warm Coastal Current in the Chukchi Sea, *Arctic*, *37*(3), 244-254.

Chao, S.-Y. (1988), River-Forced Estuarine Plumes, *Journal of Physical Oceanography*, *18*(1), 72-88, doi:10.1175/1520-0485(1988)018<0072:Rfep>2.0.Co;2.

Chapman, D. C., and S. J. Lentz (1994), Trapping of a Coastal Density front by the Bottom Boundry Layer, *Journal of Physical Oceanography*, *24*, 1464-1479.

Clement, J. L., W. Maslowski, L. W. Cooper, J. M. Grebmeier, and W. Walczowski (2005), Ocean circulation and exchanges through the northern Bering Sea—1979–2001 model results, *Deep Sea Research Part II: Topical Studies in Oceanography*, *52*(24-26), 3509-3540, doi:10.1016/j.dsr2.2005.09.010.

Coachman, L. K., and K. Aagaard (1966), ON THE WATER EXCHANGE THROUGH BERING STRAIT1, *Limnology and Oceanography*, *11*(1), 44-59, doi:doi:10.4319/lo.1966.11.1.0044.

Coachman, L. K., K. Aagaard, and R. Tripp (1975), *Bering Strait: The Regional Physical Oceanography*, University of Washington Press, Seattle, WA.

Conservation, A. D. o. E., U. S. Anchorage, and U. E. R. A. O. Office (2018), Northwest Arctic Subarea Contingency Plan, edited.

Cooper, L. W., K. E. Frey, C. Logvinova, D. M. Biasatti, and J. M. Grebmeier (2016), Variations in the proportions of melted sea ice and runoff in surface waters of the Chukchi Sea: A retrospective analysis, 1990–2012, and analysis of the implications of melted sea ice in anunder-icebloom, *Seep-Sea Research II*, *130*(6), 6-13.

Csanady, G. T. (1977), Intermittent ‘full’ upwelling in Lake Ontario, *Journal of Geophysical Research*, *82*(3), 397-419, doi:doi:10.1029/JC082i003p00397.

Csanady, G. T. (1982), On the Structure of Transient Upwelling Events, *Journal of Physical Oceanography*, *12*(1), 84-96, doi:10.1175/1520-0485(1982)012<0084:Otsotu>2.0.Co;2.

Danielson, S. L., T. J. Weingartner, K. S. Hedstrom, K. Aagaard, R. Woodgate, E. Curchitser, and P. J. Stabeno (2014), Coupled wind-forced controls of the Bering–Chukchi shelf circulation and the Bering Strait throughflow: Ekman transport, continental shelf waves, and variations of the Pacific–Arctic sea surface height gradient, *Progress in Oceanography*, *125*, 40-61, doi:10.1016/j.pocean.2014.04.006.

De Boer, A. M., and D. Nof (2004), The Bering Strait's grip on the northern hemisphere climate, *Deep Sea Research Part I: Oceanographic Research Papers*, *51*(10), 1347-1366, doi:10.1016/j.dsr.2004.05.003.

Eisner, L., N. Hillgruber, E. Martinson, and J. Maselko (2013), Pelagic fish and zooplankton species assemblages in relation to water mass characteristics in the northern Bering and southeast Chukchi seas, *Polar Biology*, *36*(1), 87-113, doi:10.1007/s00300-012-1241-0.

Elias, S. A., S. K. Short, C. H. Nelson, and H. H. Birks (1996), Life and times of the Bering land bridge, *Nature*, *382*, 60, doi:10.1038/382060a0.

Fong, D. A., and W. R. Geyer (2001), Response of a river plume during an upwelling favorable wind event, *Journal of Geophysical Research: Oceans*, *106*(C1), 1067-1084, doi:10.1029/2000jc900134.

Hallock, Z. R., and G. O. Marmorino (2002), Observations of the response of a buoyant estuarine plume to upwelling favorable winds, *Journal of Geophysical Research: Oceans*, *107*(C7), 3-1-3-13, doi:10.1029/2000jc000698.

Hasumi, H. (2002), Sensitivity of the Global Thermohaline Circulation to Interbasin Freshwater Transport by the Atmosphere and the Bering Strait Throughflow, *Journal of Climate*, *15*(17), 2516-2526, doi:10.1175/1520-0442(2002)015<2516:Sotgtc>2.0.Co;2.

Hickey, B. M., L. J. Pietrafesa, D. A. Jay, and W. C. Boicourt (1998), The Columbia River Plume Study: Subtidal variability in the velocity and salinity fields, *Journal of Geophysical Research: Oceans*, *103*(C5), 10339-10368, doi:10.1029/97jc03290.

Hu, A., and G. A. Meehl (2005), Bering Strait throughflow and the thermohaline circulation, *Geophysical Research Letters*, *32*(24), doi:doi:10.1029/2005GL024424.

Huang, R. X., and R. W. Schmitt (1993), The Goldsbrough–Stommel Circulation of the World Oceans, *Journal of Physical Oceanography*, *23*(6), 1277-1284, doi:10.1175/1520-0485(1993)023<1277:Tgcotw>2.0.Co;2.

Johnson, D. R., J. Miller, and O. Schofield (2003), Dynamics and optics of the Hudson River outflow plume, *Journal of Geophysical Research: Oceans*, *108*(C10), doi:10.1029/2002jc001485.

Johnson, D. R., A. Weidemann, R. Arnone, and C. O. Davis (2001), Chesapeake Bay outflow plume and coastal upwelling events: Physical and optical properties, *Journal of Geophysical Research: Oceans*, *106*(C6), 11613-11622, doi:10.1029/1999jc000185.

Lentz, S. (2004), *The Response of Buoyant Coastal Plumes to Upwelling-Favorable Winds*, doi:10.1175/JPO2647.1.

Lentz, S. J., and K. R. Helfrich (2002), Buoyant gravity currents along a sloping bottom in a rotating fluid, *Journal of Fluid Mechanics*, *464*, doi:10.1017/s0022112002008868.

Lentz, S. J., and J. Largier (2006), The Influence of Wind Forcing on the Chesapeake Bay Buoyant Coastal Current, *Journal of Physical Oceanography*, *36*(7), 1305-1316, doi:10.1175/jpo2909.1.

Moffat, C., and S. Lentz (2012), On the Response of a Buoyant Plume to Downwelling-Favorable Wind Stress, *Journal of Physical Oceanography*, *42*(7), 1083-1098, doi:10.1175/jpo-d-11-015.1.

Nghiem, S. V., I. G. Rigor, D. K. Perovich, P. Clemente-Colón, J. W. Weatherly, and G. Neumann (2007), Rapid reduction of Arctic perennial sea ice, *Geophysical Research Letters*, *34*(19), doi:10.1029/2007gl031138.

Paquette, R. G., and R. H. Bourke (1974), Observations on the Coastal Current of Arctic Alaska, *Journal of Marine Research 32*(2), 195-207.

Peralta-Ferriz, C., and R. A. Woodgate (2015), Seasonal and interannual variability of pan-Arctic surface mixed layer properties from 1979 to 2012 from hydrographic data, and the dominance of stratification for multiyear mixed layer depth shoaling, *Progress in Oceanography*, *134*, 19-53, doi:10.1016/j.pocean.2014.12.005.

Pisareva, M. N., R. S. Pickart, M. A. Spall, C. Nobre, D. J. Torres, G. W. K. Moore, and T. E. Whitledge (2015), Flow of pacific water in the western Chukchi Sea: Results from the

2009 RUSALCA expedition, *Deep Sea Research Part I: Oceanographic Research Papers*, *105*, 53-73, doi:10.1016/j.dsr.2015.08.011.

Rennie, S. E., J. L. Largier, and S. J. Lentz (1999), Observations of a pulsed buoyancy current downstream of Chesapeake Bay, *Journal of Geophysical Research: Oceans*, *104*(C8), 18227-18240, doi:10.1029/1999jc900153.

Roach, A. T., K. Aagaard, C. H. Pease, S. A. Salo, T. Weingartner, V. Pavlov, and M. Kulakov (1995), Direct measurements of transport and water properties through the Bering Strait, *Journal of Geophysical Research: Oceans*, *100*(C9), 18443-18457, doi:10.1029/95jc01673.

Sanders, T. M., and R. W. Garvine (2001), Fresh water delivery to the continental shelf and subsequent mixing: An observational study, *Journal of Geophysical Research: Oceans*, *106*(C11), 27087-27101, doi:10.1029/2001jc000802.

Saunders, P. M. (1973), The Instability of a Baroclinic Vortex, *Journal of Physical Oceanography*, *3*(1), 61-65, doi:10.1175/1520-0485(1973)003<0061:Tioabv>2.0.Co;2.

Shroyer, E. L., and A. J. Plueddemann (2012), Wind-driven modification of the Alaskan coastal current, *Journal of Geophysical Research: Oceans*, *117*(C3), doi:10.1029/2011jc007650.

Stern, M. E., J. A. Whitehead, and B.-L. Hua (1982), The intrusion of a density current along the coast of a rotating fluid, *Journal of Fluid Mechanics*, *123*, 237-265, doi:10.1017/S0022112082003048.

Stigebrandt, A. (1984), The North Pacific: A Global-Scale Estuary, *Journal of Physical Oceanography*, *14*(2), 464-470, doi:10.1175/1520-0485(1984)014<0464:Tnpags>2.0.Co;2.

Teledyne, R. I. (2011), Acoustic Doppler Current Profiler Principles of Operation A Practical Primer, 62.

Thomas, M., and K. Conger (2016), Coast Guard Holds Oil Spill Preparedness Training in Nome, in *The Nome Nugget*, edited, Nome.

Weingartner, T. J., S. Danielson, Y. Sasaki, V. Pavlov, and M. Kulakov (1999), The Siberian Coastal Current: A wind- and buoyancy-forced Arctic coastal current, *Journal of Geophysical Research: Oceans*, *104*(C12), 29697-29713, doi:doi:10.1029/1999JC900161.

Whitney, M. M., and R. W. Garvine (2005), Wind influence on a coastal buoyant outflow, *Journal of Geophysical Research: Oceans*, *110*(C3), doi:10.1029/2003jc002261.

Woodgate, R., K. Stafford, and F. Prahl (2015), A Synthesis of Year-Round Interdisciplinary Mooring Measurements in the Bering Strait (1990–2014) and the RUSALCA Years (2004–2011), *Oceanography*, *28*(3), 46-67, doi:10.5670/oceanog.2015.57.

Woodgate, R. A. (2011), RUSALCA-Bering Strait AON 2011 Mooring Cruise Report, 58.

Woodgate, R. A. (2018), Increases in the Pacific inflow to the Arctic from 1990 to 2015, and insights into seasonal trends and driving mechanisms from year-round Bering Strait mooring data, *Progress in Oceanography*, *160*, 124-154, doi:10.1016/j.pocean.2017.12.007.

Woodgate, R. A., and K. Aagaard (2005), Revising the Bering Strait freshwater flux into the Arctic Ocean, *Geophysical Research Letters*, *32*(2), doi:10.1029/2004gl021747.

Woodgate, R. A., K. Aagaard, and T. J. Weingartner (2005), A year in the physical oceanography of the Chukchi Sea: Moored measurements from autumn 1990–1991, *Deep Sea Research Part II: Topical Studies in Oceanography*, *52*(24-26), 3116-3149, doi:10.1016/j.dsr2.2005.10.016.

Woodgate, R. A., K. Aagaard, and T. J. Weingartner (2006), Interannual changes in the Bering Strait fluxes of volume, heat and freshwater between 1991 and 2004, *Geophysical Research Letters*, *33*(15), doi:doi:10.1029/2006GL026931.

Woodgate, R. A., T. Weingartner, and R. Lindsay (2010), The 2007 Bering Strait oceanic heat flux and anomalous Arctic sea-ice retreat, *Geophysical Research Letters*, *37*(1), n/a-n/a, doi:10.1029/2009gl041621.

Yankovsky, A. E., and D. C. Chapman (1997), A simply theory for the fate of Buoyant Coastal Discharges, *Journal of Physical Oceanography*, *27*, 1386-1401.